Faculty of Physics and Astronomy

University of Heidelberg

Diploma Thesis
in physics
submitted by

Mark Faist
born in Friedrichshafen

January 2008

Measurements on liquid helium and aluminium alloys using Neutron Radiography

This diploma thesis
has been carried out by
Mark Faist
at the
Physics Institute of the University Heidelberg
under the supervision of
Prof. Dr. Hartmut Abele

Abstract

This thesis describes an upgrading of the neutron imaging facility NEUTROGRAPH *at the ILL Grenoble and experiments performed there and at the* ANTARES *imaging station (FRM-II, Munich). A new beam limiter was installed to allow a diminishing of the neutron beam size and a collimation up to L/D>1000. Furthermore, better shielding and photon statistics for the detector are achieved with a new camera box and through geometrical optimization. A previously observed correlation between attenuation coefficient and Vickers Hardness has been further analyzed at* NEUTROGRAPH*, but could not be confirmed.*

Neutron Radiography is an excellent method to visualize transport processes and phase separation in superfluid helium mixtures because of its high statistics and the possibility to perform time-resolved measurements. These experiments have been prepared in detail at the ANTARES *imaging facility. Moreover, planned experiments and upgrades of the* NEUTROGRAPH *imaging station are discussed in this work.*

Zusammenfassung

Im Rahmen dieser Arbeit wurden die Neutronenradiographie und -tomographiestation NEUTROGRAPH *am ILL (Grenoble) erweitert sowie Experimente an dieser und an der* ANTARES*-Station am FRM-II (München) durchgeführt. Ein Beam Limiter, der eine hohe Kollimation (L/D>1000) ermöglicht, wurde installiert und ein neuer Kamerakasten für eine verbesserte Photonenstatistik und Abschirmung des Detektors wurde hergestellt. An der Station* NEUTROGRAPH *wurde zudem der Zusammenhang zwischen der Vickers-Härte und dem Attenuationskoeffizient der Neutronen bei 7449-Aluminiumlegierungen untersucht. Dabei konnte eine zuvor beobachtete Korrelation nicht bestätigt werden.*

Zur Untersuchung von suprafluiden Helium-Mischungen ist Neutronenradiographie eine hervorragende Methode, die dank ihrer guten Statistik erstmals eine Zeitaufgelöste Visualisierung von Transportprozessen und Phasenseparation ermöglicht. Hierzu wurden an der Radiographiestation ANTARES *für diese Experimente alle Vorbereitungen getroffen. Ausserdem werden in dieser Arbeit zukünftige Experimente und Ausbaumöglichkeiten für* NEUTROGRAPH *diskutiert.*

Contents

List of Figures

List of Tables

1. Introduction

This work describes upgrades and experiments performed at the NEUTROGRAPH imaging facility at ILL, Grenoble, France and at the ANTARES tomography station at FRM-II, Munich, Germany.

In Chapter 2, a short overview over the NEUTROGRAPH imaging facility and the basics of neutron radiography is given and the most important neutron imaging facilities are compared. Then, the two major upgrades of 2007, a new detector box and a beam limiter to diminish and collimate the beam are presented. At the end of the chapter, a planned collimator to lower the beam divergence is discussed.

Experiments on liquid Helium are described in chapter 3. Since similar experiments have never been done using neutron radiography, a description of the theoretical and experimental background is given. To quantificate the transport properties of superfluid helium mixtures special corrections are needed and were developed. Moreover, an experiment to observe the phase separation process of superfluid helium mixtures is proposed.

Indications of the possibility to visualize material hardness with neutron radiography have been found in a previous experiment and are further examined in chapter 4. An aluminium alloy has been artificially hardened with a heat treatment and its radiography is compared to an alloy to which no heat treatment has been applied.

Three experiments in progress are presented in chapter 5: The dynamical measurement of the TLP bonding process, a time-resolved, stroboscopic measurement of an injection nozzle and the possibility to investigate water distribution in a running fuel cell.

2. The Neutrograph imaging station

NEUTROGRAPH is a neutron imaging facility at the Institut Laue-Langevin (ILL) in Grenoble, France. It is operational since October 2002 and was built and is operated in collaboration with the "Physikalisches Institut Heidelberg" in Germany.
Due to his high flux of about $3 \cdot 10^9 n\, cm^{-2}\, s^{-1}$ it has been used for a wide range of applications including high-speed radiography and dynamic tomography.

A detailed description of the imaging facility and the physical and technical background can be found in the previous theses made at NEUTROGRAPH [Ba07, Vo06, Tr07, Sc01, Fe03, Gi03]. In this work, I will focus on the developments made in 2007.

2.1 Beam line, experimental system

The NEUTROGRAPH imaging facility is situated at the end of the ILL beam line H9, which is also used by Lohengrin (PN1), a nuclear physics station. An engineering drawing can be seen in fig. 2.1.
Lohengrin works on fission products, the setup has no influence on the measurement of the NEUTROGRAPH facility.

The beam divergence inside the casemate arises from geometry restrictions of the beam tube: the distance between neutron source and detector L and the diameter of the window to the neutron source D. It has been measured to $L/D_{horiz} = 155$ and $L/D_{vert} = 160$ [Fe03]. In optics, this represents the diameter D of the screen picture of a pinhole beam, at a distance L between screen and pinhole. A higher L/D-ratio means a better collimation and therefore a better spatial resolution.

As detector, a combination of scintillator and CCD camera (inside a camera box) is used. The scintillator, fabricated by the PSI, is sensitive to neutrons because it contains ^{6}LiF, where the ^{6}Li has a high absorption cross section for neutrons (see table 2.2). The kinetic energy of

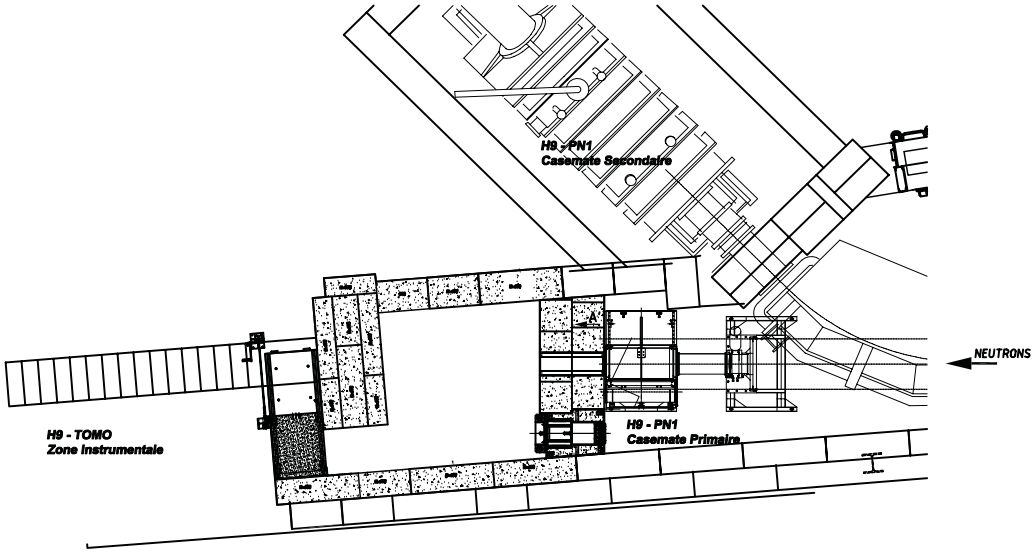

Figure 2.1: Instruments at the H9 beam line at ILL Grenoble. PN1 is the fission product spectrometer Lohengrin, TOMO the NEUTROGRAPH facility

the reaction products is transformed into visible light by ZnS, which is also contained in the scintillator. These photons are recorded by a CCD camera.
Two different cameras are used for image recording. The high-speed PCO Sensicam and the slower, but more sensitive Andor iXon DV885. A detailed comparison of the two CCD cameras can be found in [Ba07]. Unfortunately, the Andor iXon is also very sensitive to γ-radiation, which cause a pixel overflow often in several pixels. Therefore a better shielding for this camera was needed. This new design is discussed in section 2.4.1.

For sample positioning several linear and rotational tables in different sizes and accuracies are available. The whole system is modular and allows an optimized setup for each experiment.

2.2 Basics of Neutron Radiography

Radiography with neutrons is in principle a technique based on attenuation, only a few examples of phase contrast imaging exist. Neutrons passing the sample can interact with it in different ways: They can be scattered elastically and inelastically or they can be absorbed. When the sample is not close to the scintillator or its scattering cross section σ_{scatt} is not high (that means the signal from the scattered neutrons can be neglected), only the total cross section, the sum of scattering cross section σ_{scatt} and absorption cross section σ_{abs}[1], is important:

1 The absorption cross section σ_{abs} found in most tables is valid only for thermal neutrons with a velocity

$$\sigma_{tot} = \sigma_{scatt} + \sigma_{abs} \tag{2.1}$$

From now on, σ will be used as total cross section.

The total cross sections for thermal neutrons is only dependent on the interaction of the neutron with the nucleus and varies from isotope to isotope. It is particularly high for hydrogen and other light elements (e.g. Li, B) and therefore for water and other organic liquids. This fact makes neutron radiography a complementary technique to radiography with X-rays, where the cross section increases with the number of electrons (for $Z > 4$, $\sigma \propto Z^4$ is a good approximation).

The neutron attenuation coefficient is a product of the total cross section with the Avogadro number N_A and the density ρ, divided by the molar mass M, summed for each material of the sample:

$$\mu = \sum_i \frac{\sigma_i \, \varrho_i \, N_A}{M_i} \tag{2.2}$$

The intensity I of a neutron beam passing through the sample is reduced from the initial value I_0 by the following equation:

$$I = I_0 \, e^{-\mu \, l} \tag{2.3}$$

where l is the length of the sample (in direction of the neutron beam).

This neutron intensity is transformed by the scintillator into visible light (450-550nm) and is recorded by the CCD camera, which converts light intensity into a gray value. In addition to this data image, an image of the beam without sample (open beam image) must be made to correct the beam inhomogenities and a an image with closed shutter (dark image) to correct the dark current of the camera. Both correction images should be made with the same camera settings and configuration than the data image.

The transmitted intensity can then be calculated subtracting and dividing the raw data as follows (G stands for the gray values of each pixel):

of $v_0 = 2200\frac{m}{s}$ (this is equivalent to a wavelength of 1.8 Å). More correct would be the expression $\sigma_{abs} = k_n \cdot \sigma_{abs,v_0}$ with $k_n = \frac{v_0}{v}$, v being the actual velocity of the neutron. This means that cold neutrons are absorbed more easily, whereas for epithermal/fast neutrons the absorption cross section is smaller.

$$\frac{I}{I_0} = e^{-\mu\, l} = \frac{G_{data} - G_{dark}}{G_{open} - G_{dark}} \tag{2.4}$$

Equation 2.4 is only an approximation when the beam is regarded as monochromatic or beam hardening[2] is neglected. This approximation works well for standard radiography or tomography.

2.3 Comparison with other Neutron Imaging Facilities

There are several other imaging beam lines around the world, notably at the PSI/Switzerland, NIST/USA, HMI/Germany, FRM2/Germany, JRR-3M/Japan, TRIGA/Italy. The comparison in table 2.1 will be constrained of the first four of them, and for each of them only two exemplary modes of operation.

	L/D	Capt. Flux $[cm^{-2}\, s^{-1}]$	Beam $[cm^2]$	Spectrum	References
ILL	155	$3 \cdot 10^9$	400	thermal	[Hi05]
	1000	$7 \cdot 10^7$	6.3	thermal	See (2.4.2)
PSI NEUTRA	350	$8 \cdot 10^6$	660	thermal	[Neut, Le96]
	550	$4 \cdot 10^6$	1250	thermal	
PSI ICON	710	*n.a.*	104	thermal / cold	[SN05, Le07]
	1210	*n.a.*	448	thermal / cold	
FRM2 Antares	400	$9 \cdot 10^7$	1300	cold	[Ant]
	800	$3 \cdot 10^7$	1000	cold	
NIST NIF	400	$6 \cdot 10^7$	530	(epi)thermal	[Hu05]
	400	$1 \cdot 10^7$	530	thermal	
HMI CONRAD	70	$2 \cdot 10^8$	15	cold	[Hi06]
	500	$1 \cdot 10^7$	100	cold	

Table 2.1: Comparison of several Neutron Imaging Facilities

2 beam hardening is a modification in the neutron spectrum caused by neutron absorption of the sample. It is explained in more detail on page 35

Due to its high flux the NEUTROGRAPH is dedicated to study dynamic processes with a sub-millisecond time scale in stroboscopic (see e.g. [Sc06]) and up to 150fps in real-time radiography [Os04]. Tomographies can be made in less than 10s [Tr07].
PSI and FRM2 are focusing on a high spatial resolution due to its good collimation abilities: Using a cold neutron beam with thin scintillators ($10\mu m$ Gadox or $25\mu m$ Li-6 doped ZnS) a resolution better than $50\mu m$ can be achieved [Le07]. With our new setup (described in section 2.4.2, NEUTROGRAPH can achieve the same spatial resolution, combined with a better penetrating capacity.

2.4 Upgrading in 2007

Due to the relatively high beam divergence and Gamma background compared to other Neutron Imaging instruments, we optimized the setup of the NEUTROGRAPH imaging station. I will discuss two big modifications made in 2007:
With the new camera setup (2.4.1), a better protection of the CCD-Camera is achieved while the distance between lens and scintillator screen is shortened, enhancing light efficiency by a factor of 2.7.

A new beam limiter (2.4.2) allows to reduce the beam size arbitrarily up to a pinhole, which leads to a $L/D \geq 1000$ with a small beam diameter (25mm $\times$ 25mm), still preserving a relatively high flux of $7 \cdot 10^7 n\, cm^{-2}\, s^{-1}$. For such a L/D and a distance between scintillator and sample of $d < 5cm$ the spatial resolution is not longer determined by the beam divergence but by the resolution of the scintillator. Therefore, further detector development is needed.

2.4.1 Camera Box

The reaction of neutrons with the sample (or the experimental setup) produces γ - photons (typically keV - MeV), which can reach the CCD chip and lead to pixel overflows. They can be filtered well in picture series [Ba06], but a lot of computing time and memory is needed because pictures can't be accumulated directly. For a fast tomography, moreover, only one picture per angle can be made and a such a filtering is not applicable.

To protect the camera from the majority of γ-rays, about 15-20cm of lead protection is needed, this attenuates a MeV photon beam by 10^{-4} [NDB01].

Previous Setup

The previous camera box [Gi03] consists basically out of two mirrors in an opaque box (U-shape) (See figure 2.2). There are two middle parts (connectors) to vary the optical path length between scintillator and camera.

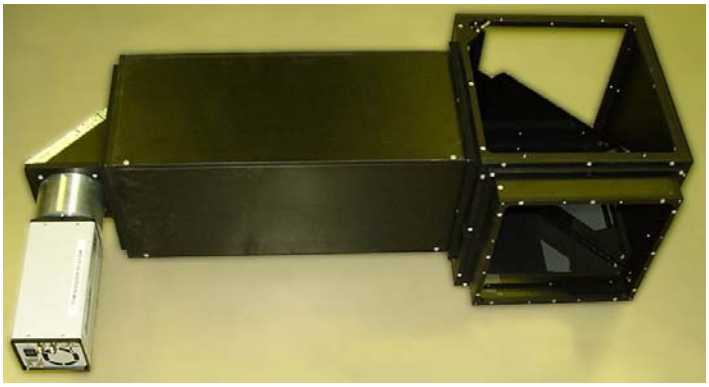

Figure 2.2: Previous camera box in the long option

The main disadvantage of this box is that the camera is aligned with the sample. This makes it difficult to place enough lead between sample and CCD-Chip, especially when the box is used with the short connector, so for most experiments only the usage of the long connector is feasible. Moreover, the Andor iXon 885 is sensible to γ - radiation making its protection more important.

New Design

The new camera box resolves this problems by using the third dimension and by optimizing the angle between neutron beam and first mirror. This leads to the fact that the new camera box is easier to handle with a 60cm distance between lens and scintillator instead of more than 100cm for the old camera box. Since the photon statistics are proportional to d^{-2} the light statistics are increased by a factor of 2.7, so the EMCCD intensifier can be run at a lower amplification factor.

The most visible difference is the vertical alignment of the camera. This makes it possible to protect the camera with much more lead without losing space in the sample area. All pieces are now on an aluminium plate, the scintillator is the object closest to the beam window. To achieve this, the first mirror is mounted at 50° with respect to the neutron beam, redirecting the light more backwards than the plane perpendicular to the beam (see figure 2.3a). It is cut

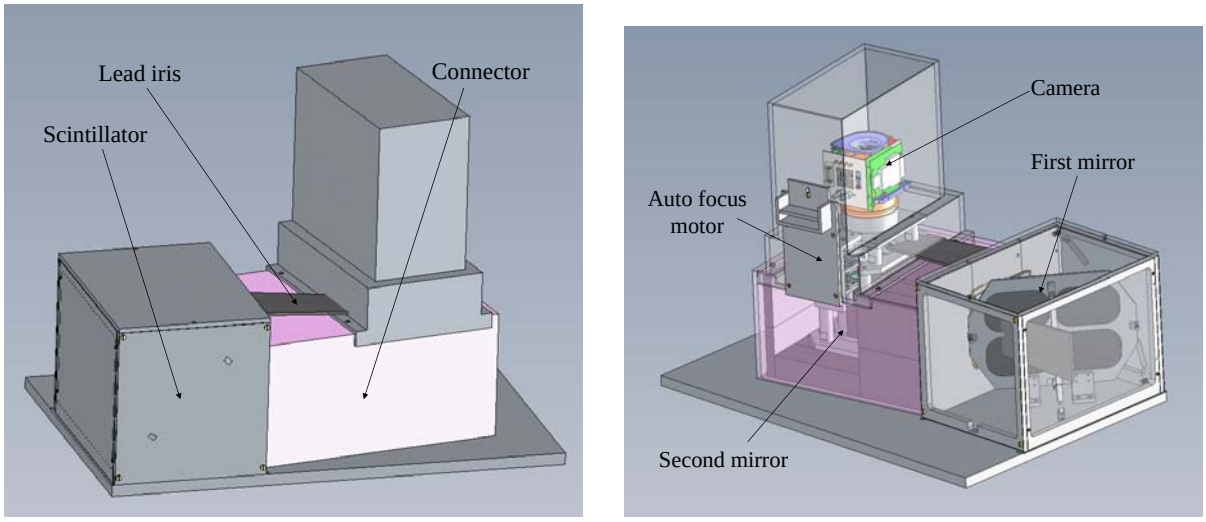

(a) Front view on the camera box

(b) back view with insight

Figure 2.3: Design of new camera box. The lead is not visible in the figure

out of a 30cm-diameter Si crystal and mounted on an aluminium fixture.

Inside the connector in between the two mirrors, the light passes through a special iris made out of lead, where only an opening with the size of the light beam is left. This piece absorbs the γ-rays produced at the first mirror and its fixture. The second mirror is placed at the end of this piece.

To achieve an always minimal distance between second mirror and lens, different mountings are available for different lenses and are directly connected to the mirror fixture. All lenses can be connected to an auto focus motor, hence direct focusing to the scintillator light will be possible for the first time. This eliminates errors caused by the different thickness of scintillators or differences between scintillator and test mask position.

To lengthen the distance between scintillator and camera, e.g. when a bigger field of view is needed, two extensions with the length of 20cm and 40cm are available and allow a scintillator distance of 80cm, 100cm and 120cm.

2.4.2 Beam Limiter

Before the upgrading in August 2007, there was no possibility to reduce the beam dimensions from its original size of $210mm \times 210mm$. This lead to many disadvantages: Neutrons scat-

tered by the experimental setup, the camera box or the air hit the scintillator and diminish the S/N-ratio. Parts of the scintillator not needed for the measurement are hit by the beam and degrade. Moreover, the items inside the casemate become less active when the neutron beam is reduced.

The beam limiter has been installed as far as possible from the scintillator, directly after the Lohengrin dipole magnet (see figure 2.1), to achieve the best beam collimation.

Materials and Properties

To reduce the beam size and so confine the neutron impact to the desired area, several materials with a high neutron absorption cross section can be put into the beam. Table 2.2 gives a short overview of different materials.

Element (Isotope)	$\sigma_{abs}[barn]$	Reaction
$Li\ (^6Li)$	71 (940)	$^6Li + n \rightarrow ^3H + \alpha$
$B\ (^{10}B)$	767 (3835)	$^{10}B + n \rightarrow ^7Li + \alpha + \gamma(0.48MeV)$
$Cd\ (^{113}Cd)$	2520 (20600)	$^{113}Cd + n \rightarrow ^{114}Cd + \gamma$
$Gd\ (^{157}Gd)$	49700 (259000)	$^{157}Gd + n \rightarrow ^{158}Gd + \gamma$

Table 2.2: Different neutron absorbing elements [NDB01]

Gadolinium and Cadmium are the materials with the best attenuation characteristics, but the absorption of neutrons is accompanied by emission of high energy γ-rays and poses problems to the radioprotection. Therefore it is not convenient to use them directly in a high flux beam. The reaction of ^{6}Li with neutrons produces only few γ-rays (10^{-4} suppression) and can be used to get a sufficiently high neutron absorption. It is available as ^{6}LiF that can be cast in silicone rubber (up to 7%).

For our purpose the best suited material is Boron in the form of Boron Carbide (B_4C) with $\sigma_{abs} = 600$ barn. It is available in 7mm-thick plates, each of them reduces the thermal neutron intensity by a factor of 10^{-5} [AZOM]. The intensity of the γ-rays produced by Boron can be reduced by a factor of 100 with 3cm of lead. Boron Carbide is not easily machinable because of its extreme hardness, but it can be sawn with very sharp edges which make it possible to

approach even big plates to distances smaller than $1mm$

In our setup, four B_4C plates (145mm×290mm×7mm), each connected to a ISEL linear guide are mounted vertically (See figure 2.4). Each plate can be moved separately with a stepper motor, every position and opening within the neutron beam can so be chosen through a software interface (see section 2.4.2). The positioning precision (one step of the motor) is 75μm at a minimum opening of around 1mm.

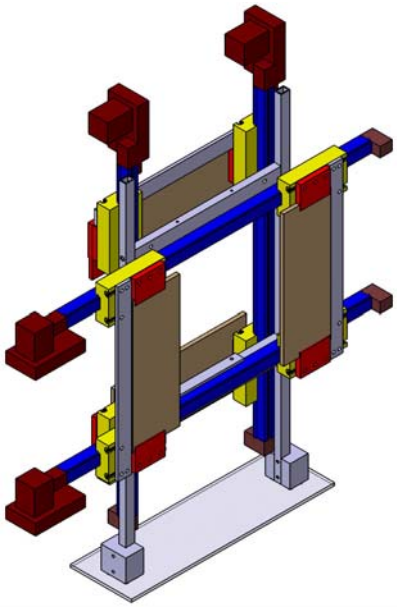

Figure 2.4: Design of Beam Limiter

Modes of Operation

The beam limiter can be used for two purposes. The diminution of the beam size and the augmentation of the L/D ratio (pinhole mode).

For the pinhole mode, the plates are set to stay close (distance 1-28mm), leaving only a small quadratic opening. Similar to a pinhole camera one gets an inverted reproduction of the source (see fig. 2.5). In figure 2.6 the beam size is reduced to a plateau size of 50mm x 50mm.
The pictures 2.5 and 2.6 are a sum of 20 exposures (exp. time 1s), only corrected by subtracting a dark image.

Different $\frac{L}{D} = \frac{opening}{distance\ to\ scintillator}$ can be achieved with different apertures (fig. 2.7). Compared to other Neutron imaging facilities, NEUTROGRAPH has still the highest flux at an L/D ratio

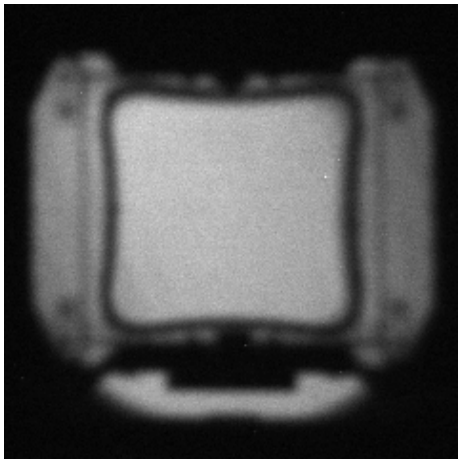

(a) pinhole picture on the scintillator

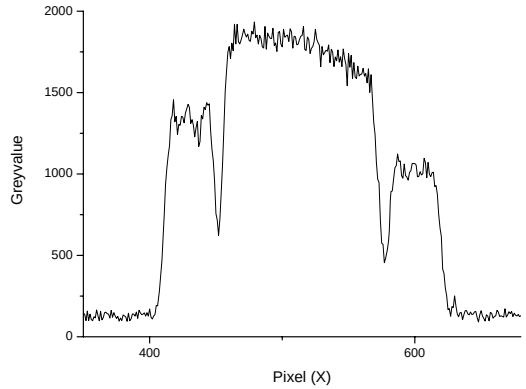

(b) Gray values of pixel line 551

Figure 2.5: Reproduction of the source (opening $2mm$). In addition to the source, effects of the Lohengrin dipole magnet (below the source) and shutter (left and right) can be seen.

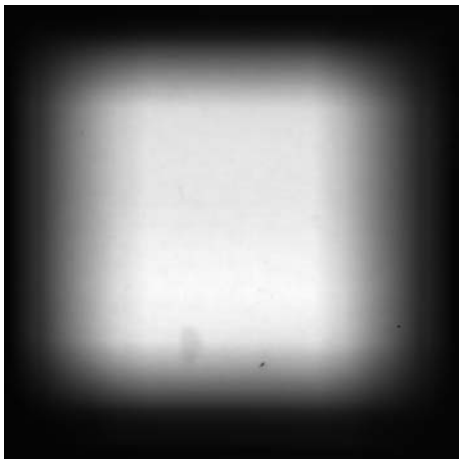

(a) picture on the scintillator

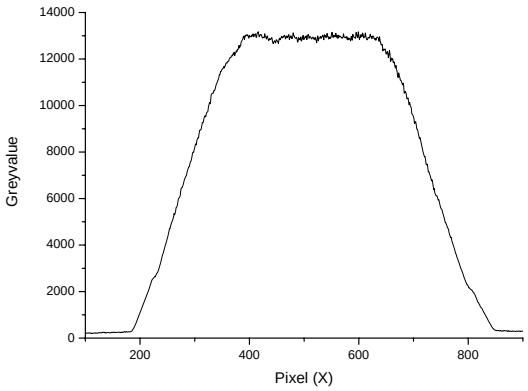

(b) Gray values of pixel line 551

Figure 2.6: Smaller neutron beam with plateau (opening $80mm$)

of 1000 (See table 2.1).

As can be seen in figure 2.1, the fact that the beam line H9 is used by Lohengrin leads to a spatial constraint: All equipment (e.g. shutters, apertures) must be placed after Lohengrins dipole magnet (distance to the casemate: 2m). This leads to geometrical disadvantages: The distance between the beam limiter and the scintillator is restricted by the size of the casemate (L $<$ 4m) and at a high L/D the size of the beam becomes very small. For openings larger than 28mm the L/D-ratio is no longer determined by the beam limiter but by the geometry neutron source and distance between source and detector.

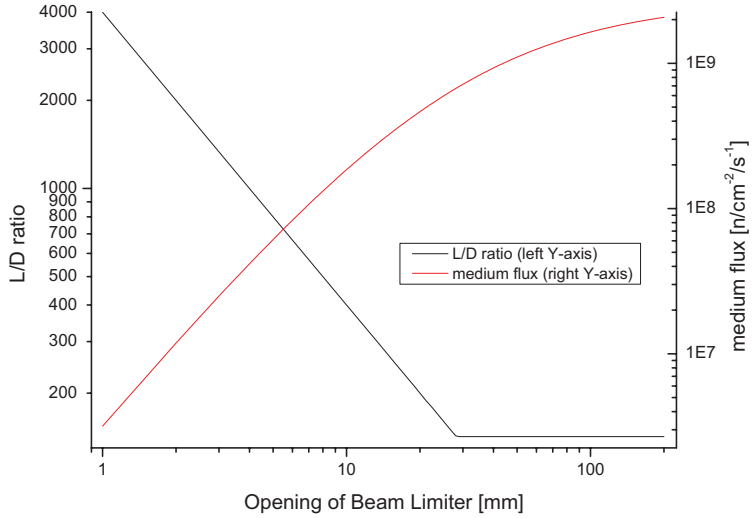

Figure 2.7: Different operation modes of the beam limiter. The value on the x-axis is the side length of the quadratic opening

Software interface

The four plates of the beam limiter are synchronized automatically through an ISEL controller box and a software interface. The only input needed by the software is the position of the beam limiter opening (the origin is the middle of the beam) and the horizontal and vertical opening. After a click on ***Move***, the plates move to the desired position. With the buttons ***Move in*** and ***Move out***, the beam limiter is set to its smallest (1mm x 1mm) or largest (230mm x 240mm) opening. When the program is closed, all current settings are saved to a file and are automatically reloaded at a restart of the software interface. When there is a longer break between two beam cycles, the button ***Shut down*** should be pressed to move the plates to a position where the controller box can be switched off.

2.5 Upgrades in progress

2.5.1 Soller - Collimator

Since there are geometric restrictions from the instrument PN1 at the H9 beam line, the L/D ration cannot be enhanced by collimating the beam close to its source. A set of two soller collimators is a possibility to increase the L/D ratio preserving a large beam size.

A soller collimator is a stack of parallel metal plates or Mylar foils with spacers between the foils for a parallel alignment. The foils are coated with a neutron absorbing material, e.g. ^{10}B

or ^{157}Gd, so that almost all neutrons touching a foil are absorbed. The surface of the foils should be rough to avoid reflection of cold neutrons. If this two conditions are met, the L/D ratio of the beam is determined by the thickness of the spacers and the length of the collimator. It must be noted, however, that a horizontal and a vertical collimator is needed.

Initially, soller collimators with a L/D-ratio of around 600 were planned, but it was not possible to produce them for the beam size of NEUTROGRAPH. A collimator from the now planned set consists out of 170 Al foils with the thickness of 125μm (spacers thickness: 75μm). The field of view is planned to be 150mm x 150mm with a collimator length of 500mm. This would enhance the L/D-ratio to 330, when it is measured with the method of Kobayashi. But the spatial resolution depends not only on the L/D-ratio, but also on the angular distribution of the neutron beam, which is considerably changed by the soller collimators (see fig. 2.8).

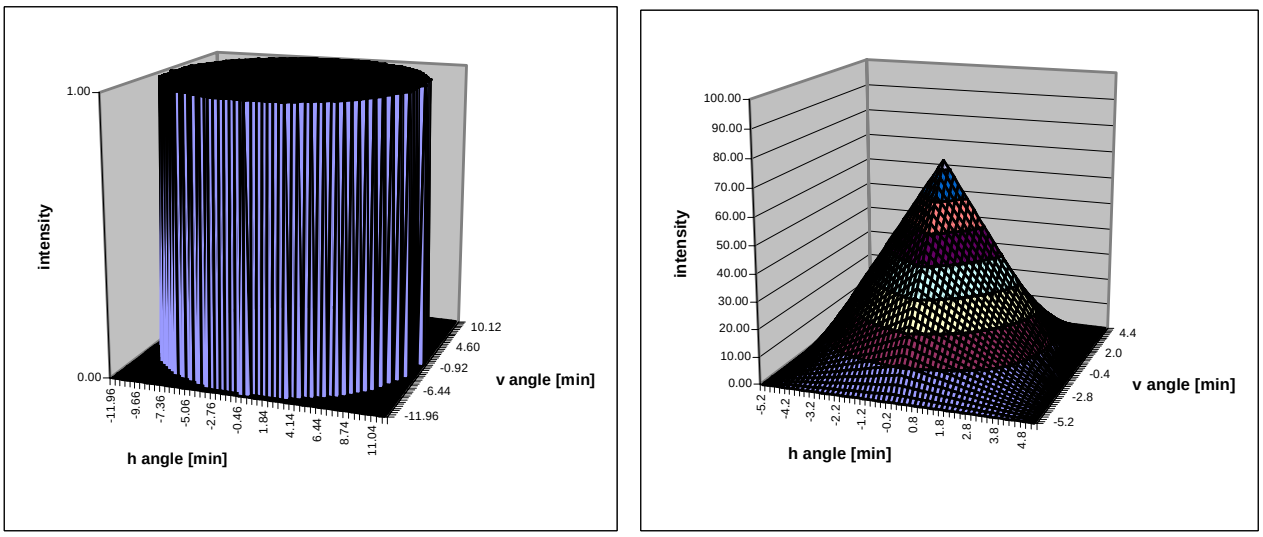

Figure 2.8: Calculated angular distribution of the uncollimated beam (left) compared to the angular distribution after the planned soller collimator (right) (from [Vo07]). The loss in intensity for an angle of 0° of the soller collimated beam corresponds to the loss in the beam due to the finite thickness of the foils.

The uncollimated beam is only geometrically restricted by the diameter of the sourch and the distance between detector and source. This geometry eliminates all neutrons with a divergence greater than $\pm 11.5\, mrad$. The remaining intensity is equal for all angles allowed by this geometry (see fig. 2.8). The case is different for the soller collimator. Here, small angles are preferred, but also some neutrons with a fairly high divergence can pass. This leads to the pyramidal form of the angular distribution. It follows that the spatial resolution of these two

different distributions cannot be simply compared with the L/D-ratio.

To compare the two angular distributions, a simulation of three beams has been made: two uncollimated beams (L/D=300, L/D=600) and a soller collimated beam with a L/D-ratio of 300. A virtual test mask consisting of neutron absorbing stripes with the thickness 1mm-2mm-3mm-...-10mm has been put in the virtual beam and the difference in absorption measured by a scintillator in 5cm distance has been compared for the different neutron beams. The result can be seen in figure 2.9.

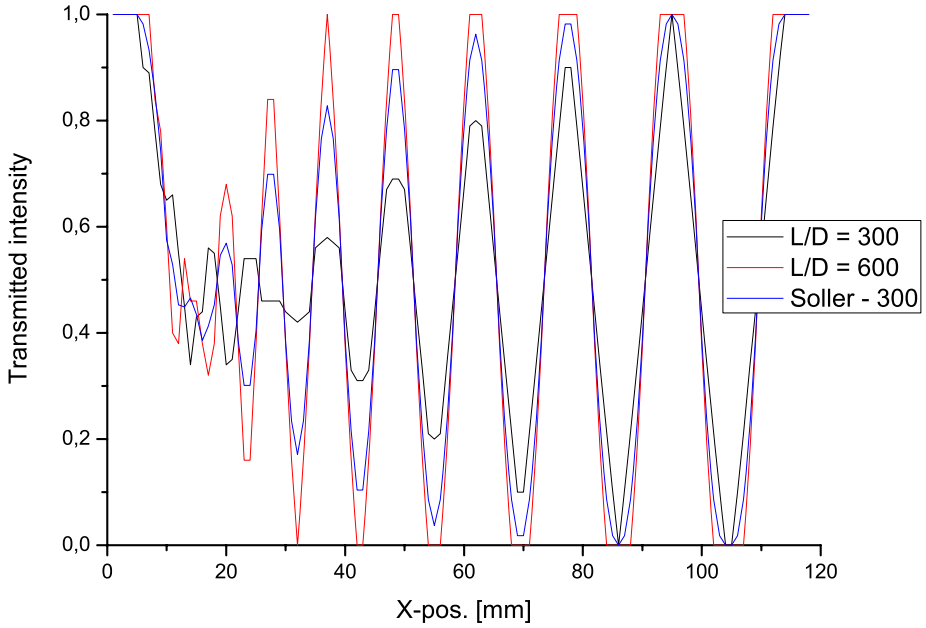

Figure 2.9: Comparison of the spatial resolution of the soller collimated beam with two different uncollimated beams.

For the Kobayashi measurement, only the peak at X-pos. 95 in fig. 2.9 is taken into account. There, both neutron beams achieve the maximal intensity of transmission. Hence the L/D ratio of both is 300. The form of the peak, however, is not taken into consideration. For the spatial resolution, however, it is of major importance. The resolution of the soller collimated beam is much closer to the resolution of the L/D=600 uncollimated beam.

3. Experiments on liquid Helium

Over the last 50 years, there have been several motivations to observe liquid helium. In 1962, H. London proposed a scheme for dilution refrigeration, in the early 1970's the superfluidity of ^{3}He was discovered. Recently, the ^{3}He-^{4}He mixtures became important for the measurement of the electric dipole moment of the neutron. As stated by R. Golub, the properties of dilute ^{3}He-^{4}He mixtures are important for a search of the neutron EDM in superfluid ^{4}He with polarized ^{3}He [Go94].

With our experiments, we want to observe transport processes in superfluid ^{3}He-^{4}He mixtures to measure the mass diffusion coefficient and visualize the phase separation. The experiments on liquid Helium were performed in December 2007 at the ANTARES imaging facility at FRM-II because of the availability of the ^{3}He-cryostat and the good support.

In section 3.3, the experiment to measure of the mass diffusion coefficient of ^{3}He in ^{4}He is described. In addition, an experiment to observe the phase separation process is proposed (section 3.4). The decomposition of the mixture has not yet been visualized, our method allows a measurement with a frame rate up to 30fps, depending on the intensity of the neutron beam. Possible improvements for future experiments are described in section 3.5.

3.1 Motivation

The mass diffusion coefficient of ^{3}He in superfluid ^{4}He has been precisely measured for $T > 1.4K$ [Mu97], whereas below this temperature, only one measurement with a precision of 20% exists for the temperature range from 0.45K to 0.95K (figure 3.1) [La02]. With our method, the precision of this data can be increased and new values can be measured in the temperature range from 0.95K to 1.4K.

The observation of the phase separation process of superfluid and normalfluid helium mixtures can lead to deeper insight in the process of phase separation and critical behaviour.

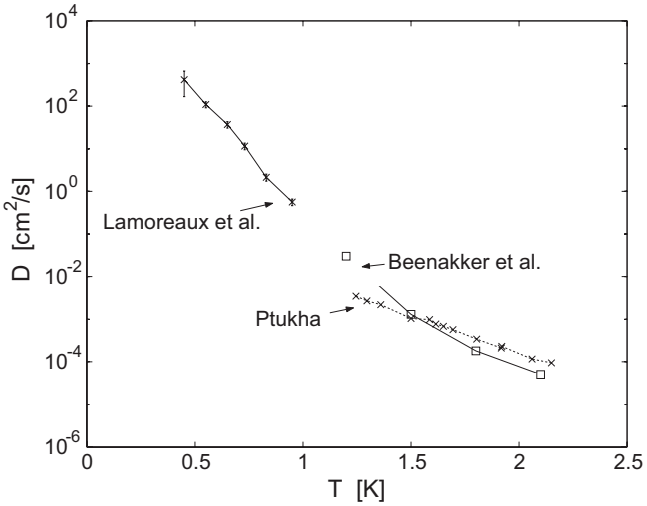

Figure 3.1: Comparison of different measurements of the mass diffusion coefficient of ^{3}He in ^{4}He, from Ptukha [Pt61], Beenakker et al. [Be52] and Lamoreaux et al. (from [La02])

With neutrons it is possible to probe the ^{3}He-concentration with high resolution because of the extremely high difference in the cross section between the different helium isotopes (see table 3.1).

Isotope	$\sigma_{scatt}[barn]$	$\sigma_{abs}[barn]$	$\sigma_{total}[barn]$
^3He	6.0	5333.0	5339.0
^4He	1.3	0.0	1.3

Table 3.1: Cross sections of thermal neutrons with the different Helium isotopes [NDB01]

^{4}He is almost invisible for Neutrons, ^{3}He captures them

$$^3He + n \longrightarrow {}^3H + p + e^- \tag{3.1}$$

with an energy release of 784 keV, mostly in recoil energy of triton and proton. For liquid ^{3}He with a density of 0.059 $g\,cm^{-3}$ (at boiling point) follows an attenuation coefficient for thermal neutrons of μ=63.7 cm^{-1}. That means, after passing through only 0.36mm of (pure) liquid ^{3}He, 90% of the neutrons are absorbed. Hence for experiments with neutrons only very low ^{3}He densities or very thin experimental volumes are feasible.

We use both approaches in two different experiments: the observation of transport processes in dilute Helium-mixtures (section 3.3) and the phase separation process in mixtures with much higher ^{3}He concentrations (section 3.4).

3.1.1 Preliminary experiment

A dynamic radiography of channels in a dilution refrigerator has been made as preliminary experiment in 2004 at the NEUTROGRAPH. Dynamic radiographies of capillaries filled with ^{3}He-^{4}He-mixtures have been made and the phase separation has been observed. Figure 3.2 shows such a radiography. On the bottom left, two capillaries with pure ^{3}He and ^{4}He are mixed, the separated phases can be observed in the capillary on the right.

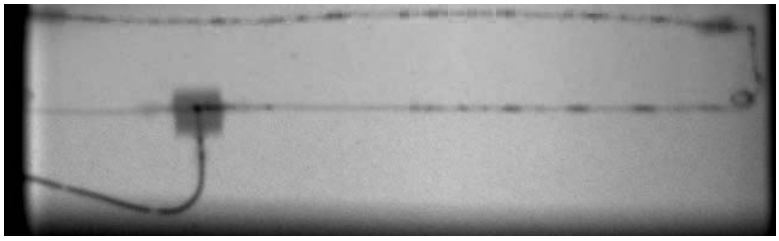

Figure 3.2: Neutron radiography of Helium-mixtures, recorded in 2004 at NEUTROGRAPH

This preliminary experiment showed the extraordinary contrast between ^{3}He and ^{4}He not achievable with other imaging methods.

3.2 Setup

In this section, the general setup used for both experiments is described. More specific considerations are made in the sections *Experimental technique* of each experiment (section 3.3.2 and 3.4.2).

For our experiment we used a ^{3}He cryostat because of its bigger cooling power compared to a dilution fridge at our temperature range (see fig. 3.3). The FRM-II sample environment provided a ^{3}He-insert inside a closed cycle refrigerator (CCR-1). This cryostat has a cooling power of about 350mW down to 3.6K and its ^3He inset cools with 3-5mW down to 0.6K. The base temperature of the system is 450mK. The vacuum can of the ^{3}He-insert has an inner diameter of 42mm, the maximum height of the experimental volume is 72mm.

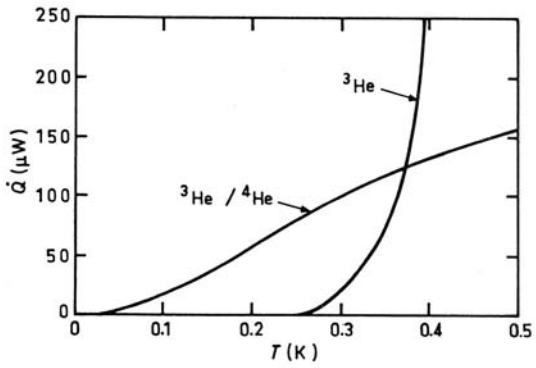

Figure 3.3: Cooling power of a ^{3}He-cryostat compared to a ^{3}He/^{4}He dilution fridge (from [Lo74])

The cryostat was modified for our purpose: the experimental chamber was connected to the outside through a capillary, so that the helium-mixtures could be condensed in. This capillary was connected through a small Swagelok system to a gas cylinder and to the exhaust pipe. The latter is necessary to avoid the contamination of the experimental hall with tritium.

Figure 3.4: The final setup at ANTARES

Inside the casemate the cryostat was mounted on a X-Z and rotational table (see picture 3.4). With this setup, it is possible to align the rectangular experimental volume with the beam

and to move the cryostat out to make an open beam image needed for the correction of the scintillator degradation.

The neutron beam at ANTARES has a thermal/cold spectrum (see fig. 3.15), at L/D=400 the flux is $9 \cdot 10^7\ n\ cm^{-2}\ s^{-1}$. Before entering the casemate, the beam size is reduced by a beam limiter to minimize the activation and neutron heating [Ant].

An Andor DW436 CCD camera is used for image recording. It features a high quantum efficiency ($> 90\%$ for the wavelength of the scintillator light), a 1 Mhz pixel readout rate and 4 Megapixels. A LEICA APO-MACRO-ELMARIT 100mm macro lens is used to achieve a high spatial resolution.

3.3 Transport processes of ^{3}He in He-II

3.3.1 Theory

In 1938, the first evidence of flow without dissipation, called superfluidity, was announced [Al38]. Since then, research on superfluid Helium, named Helium-II, or more general on quantum fluids, has become an important field of research. The two stable Isotopes of Helium behave very differently at low temperatures, because ^{4}He is a boson whereas ^{3}He is a fermion. ^{4}He becomes superfluid below the transition temperature $T_\lambda = 2.17K$, ^{3}He has a superfluid phase only at very low temperatures, where the ^{3}He atoms couple to cooper pairs.

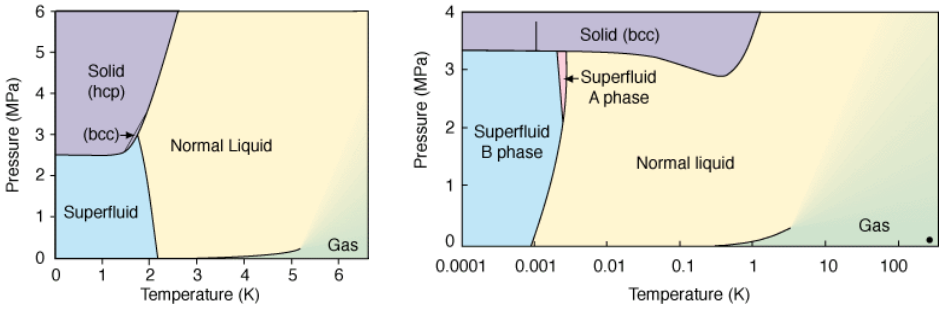

Figure 3.5: Phase diagrams of the two isotopes ^{4}He (left) and ^{3}He (right, with logarithmic temperature scale) [Al05]

Despite of extensive research in this field it has proven difficult to monitor the transport properties of Helium-II, due to its property of "self-cleaning": every other atomic species is expelled from its bulk. This makes it remarkably difficult to use ions or other atoms as tracer particles.

Using ^{3}He as impurity does not pose this problems. It has been shown in [La49] that ^{3}He dissolved into ^{4}He couples to the normal component of the solution (section 3.3.1), this allows to observe the transport processes in He-II directly.

For temperatures below $T_\lambda = 2.17K$, liquid ^{4}He behaves in many ways like a composition of two separate fluids, one of which carries no entropy and has no viscosity. London explained most of its behaviour with the two-fluid-model [Lo38]. The theoretical background of the two-fluid model is needed to explain the transport properties and extract the mass diffusion coefficient from the ^3He distribution.

Two-fluid-model

Since ^{4}He is a boson (totally symmetric wave function), there is no restriction for the number of ^{4}He-Atoms in the ground state. By neglecting the interatomic forces, the liquid can be described (as ideal gas) with the Bose-Einstein distribution function,

$$f_i = \frac{1}{e^{(E_i-\mu)/k_BT} - 1} \tag{3.2}$$

being f_i the probability that a state of Energy E_i is occupied. k_B is the Boltzmann constant and μ the chemical potential. As temperature is reduced, more and more particles are occupying the ground state, which carries no entropy.
The two-fluid-model is based on this assumption, though it is a macroscopic, phenomenological model. As long as temperature gradients, velocities etc. do not grow too large, He-II can be treated as composition of a normalfluid and a superfluid liquid, none of them interacting with the other. The following assumptions can be made [Wi67]:

- the density ρ of the liquid is the sum of the densities of both components: $\rho = \rho_s + \rho_n$, where ρ_s is the density of the superfluid and ρ_n the density of the normalfluid component. $\rho_n = 0$ at $T = 0$, and ρ_s=0 at $T = T_\lambda$ (see figure 3.6)
- the superfluid component (subscript s) carries no entropy and has no viscosity or turbulences, being $\nabla \times v_s = 0$
- the normal component (subscript n) carries the whole entropy S of the liquid

With the two-fluid-model it is possible to describe many properties of liquid helium in the linear regime, although numerical quantities such as ρ_s or ρ_n must be determined by experiment.
One prediction is the enormous thermal conductivity, since the two-fluid-model allows an unusual form of convection: at the heater the superfluid component is converted to the normalfluid

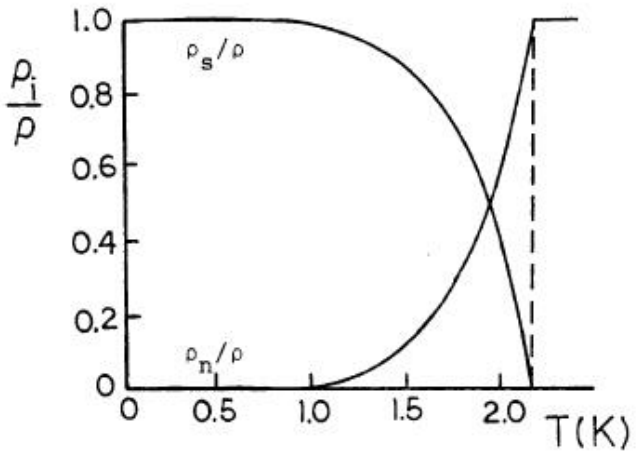

Figure 3.6: Superfluid and normalfluid densities of the two-fluid-model, measured by Andronikashvili (1946) by immersing a stack of disks into the liquid helium used as a torsion pendulum [Cl92]

one, which flows to the heat sink. There it releases all of its entropy and is re-converted to superfluid, which flows back to the heater, not interacting with the normal fluid. This leads to a particularly high heat conductivity, much higher than the conductivity of Helium-I.

On the other hand, it does not explain the superfluidity itself, so a more detailed level must be considered (see below).

Excitations in Helium-II

Landau proposed 1941 to describe the properties of He-II in terms of elementary excitations, phonons and rotons. He proposed a dispersion curve similar to the one in fig. 3.7, measured later by neutron scattering.

Important for temperatures not too close to the λ-point are two regions: at temperatures below 0.6K mostly the phonon region with the dispersion relation

$$\epsilon = cp \tag{3.3}$$

(c is the velocity of sound, ϵ the energy and p the momentum) is populated. At higher temperatures the rotons, excitations in the "minimum region" become more important. They have the dispersion relation

$$\epsilon = \Delta \cdot \frac{(p - p_0)^2}{2\mu} \tag{3.4}$$

with Δ, μ and p_0 as three experimentally determined constants. It must be noted, that there is

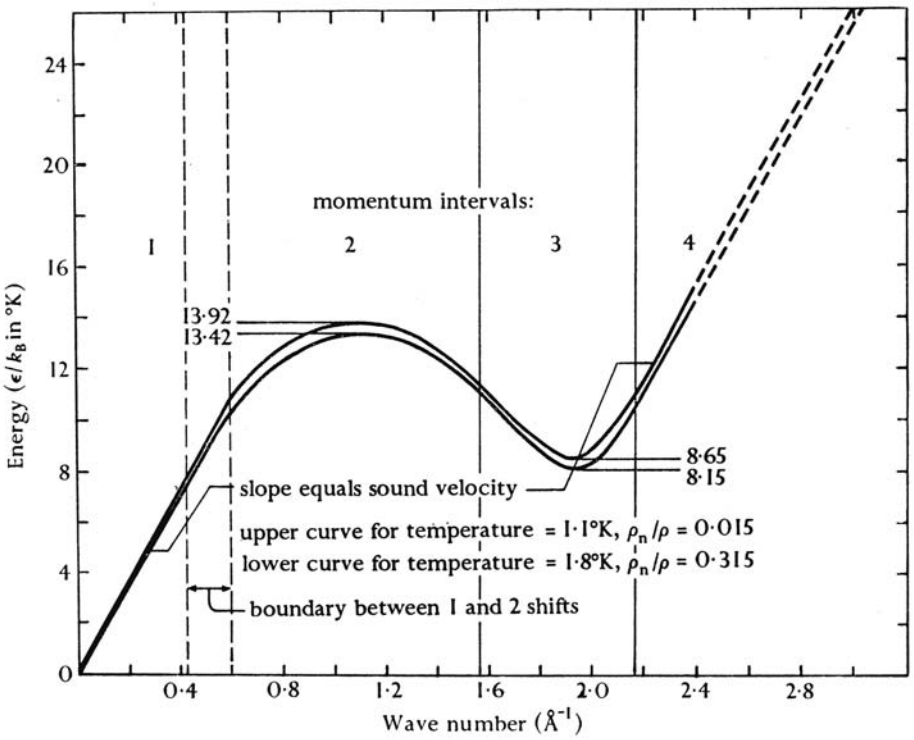

Figure 3.7: The He-II dispersion relation divided into different intervals. Interval 1 is the phonon region, interval 3 the roton region (from [Wi67])

no connection between rotons and rotation, the name has only a historical background, because equation 3.4 was derived by Landau from hydrodynamics.

Thermodynamically, the excitations are expressed by the entropy $S(T, P)$ of the liquid, a constant for given temperature and pressure. The entropy increased with the temperature as new regions of the dispersion curve can be populated. It has been shown, that the normalfluid component (of the two-fluid-model) is in fact a representation of these excitations (see [Cl92], p.174).

Dilute solutions of ^{3}He in ^{4}He

In this work, mixtures of ^{3}He in ^{4}He are considered dilute as long as the interaction between the ^{3}He atoms is neglectable, a good approximation for a molar ^{3}He-concentration $X < 10^{-2}$ (in our temperature range). The molar ^{3}He concentration X is the number of ^{3}He atoms n_3 divided by the number of atoms in the mixture $n_3 + n_4$:

$$X = \frac{n_3}{n_3 + n_4} \tag{3.5}$$

Already small concentrations of ^{3}He in ^{4}He can change the physical properties significantly, especially for very low temperatures, where the ^{3}He atoms behave as fermions. For our experiment the change in thermal conductivity is particularly important. As first measured by Ptukha [Pt61], the thermal conductivity lowers drastically with increased ^{3}He-concentrations, leaving it several orders of magnitude below the value for ^{4}He [Ab68]. Figure 3.8 shows the effective thermal conductivity for different ^{3}He-concentrations.

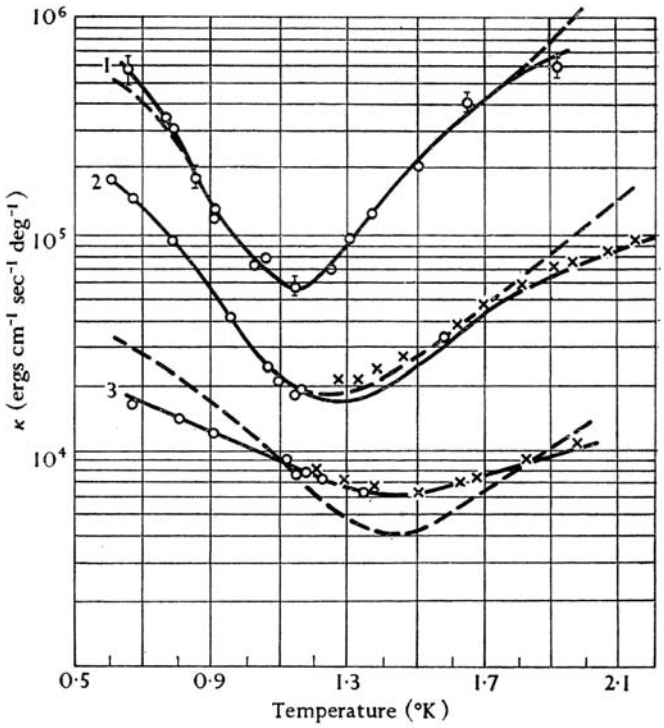

Figure 3.8: The effective thermal conductivity of dilute ^{3}He-^{4}He-mixtures: curve 1, $X = 1.4 \cdot 10^{-4}$; curve 2, $X = 1.3 \cdot 10^{-3}$; curve 3, $X = 1.36 \cdot 10^{-2}$ (from [Pt61])

The saturated vapour pressure (SVP) increases with the ^{3}He-concentration, because liquid ^{3}He is much more volatile than liquid ^{4}He. It is coupled to He-II with an energy of only 2.8K, so when the gas is in equilibrium with the liquid, its ^{3}He concentration is higher.

Attention must be given to these and other corrections in order to obtain a high precision in the experiment (they are discussed from page 30 on). Often, only poor data is available for dilute mixtures, e.g. the thermal conductivity data seen in figure 3.8. This can lead to further inaccuracies.

It has been shown, first by Daunt et al. [Dau47], that ^{3}He atoms do not take part in the superfluid motion and therefore don't interact with the superfluid component. ^{3}He is so carried along with the normalfluid flow, which eventually makes it possible to observe the fluid dynamics of superfluid Helium (page 26) through contrast differences in neutron radiographies.

More general considerations on fluid He-mixtures will be made in section 3.4.1.

Measurement of the mass diffusion coefficient

According to Beenakker et al., the heat flow in superfluid Helium is carried by a flow of thermal excitations [Be52]. In terms of the two-fluid-model, this can be written as

$$\dot{\mathbf{Q}} = \rho S T \mathbf{v}_n \tag{3.6}$$

where $\dot{\mathbf{Q}}$ is the heat flux, ρ the density, S the entropy, T the temperature and v_n the normalfluid velocity. When the liquid is isothermal and at constant pressure, S and ρ are constant.
When a heat source is introduced, the normal component starts to move towards the heat sink. The ^{3}He scatters with the excitations (page 23) and accelerates. Due to the high effective mass $m_3^* > m_4$ the reaction of ^{3}He is delayed, but in the steady state it reaches the same velocity than the Helium-II and accumulates at the heat sink. Another effect is the backscattering of ^{3}He from the background phonons, described by the mass diffusion coefficient. These two effects lead to a redistribution of the ^{3}He concentration X following the equation

$$X\mathbf{v}_n - D\vec{\nabla}X = 0 \tag{3.7}$$

with D as mass diffusion coefficient.

From the conservation of entropy, we get

$$\frac{\partial \rho S}{\partial t} = -\vec{\nabla} \cdot \rho S \mathbf{v}_n = 0 \tag{3.8}$$

in steady state. This leads to $\vec{\nabla} \cdot \mathbf{v}_n = 0$. In the two-fluid-model approximation, where no turbulences occur, we can assume $\vec{\nabla} \times \mathbf{v}_n = \mathbf{0}$. These two assumptions allow us to introduce a

velocity potential Φ which satisfies the Laplace equation $\Delta\Phi = 0$.

The solution for equation (3.7) is then

$$X = C\, e^{\Phi/D} \tag{3.9}$$

where C can be determined by integrating over the experimental volume: $\int Ce^{\Phi/D}\, dV = X_0 \cdot V$, assuming the conservation of the ^{3}He-atoms in the liquid (valid for a negligible vapour volume).

The mass diffusion coefficient can so be determined by measuring the spatial distribution of ^{3}He as function of an externally applied heat flux $\dot{\mathbf{Q}}$, when there is a simple dependence $\Phi(\dot{\mathbf{Q}})$.

More detailed calculations, including our experimental conditions, will be made in section 3.3.2, including estimations on the validity of our approximations.

3.3.2 Experimental technique

A measurement of the spatial distribution of ^{3}He is made by means of Neutron Radiography. Dilute ^{3}He-^{4}He-mixtures are condensed into an experimental volume. At its bottom, a heat flux is applied and the concentration difference in ^{3}He is measured through neutron absorption. The LINDE gas mixtures had a ^{3}He-concentration of 903ppm and 3056ppm. Two different gas mixtures have been ordered to observe any concentration dependence of the mass diffusion coefficient. In previous work, it has been found to be independent [La02, Mu97].

Experimental volume

As the integrated absorption is being measured along the neutron beam, it would be best to have a constant ^{3}He-concentration for constant z. To achieve that, we use an experimental volume of copper and steel (See fig. 3.9). Bottom (heat source) and top (heat sink) are out of copper, the side walls are fabricated of stainless steel 4571. Due to the low thermal conductivity of stainless steel all but a neglectable part of the heat flow goes through the Helium-mixture.
A 100Ω-resistance was used as heat source, connected to a constant-current source (0-100mA). The heating power is measured with the help of a four-wire circuit by two KEITHLEY 2000 multimeters. Additional to the heat source, a Lakeshore CX-1030-CU-0.3B thermometer was mounted to the bottom of the cell to observe the temperature difference between bottom and top.
For the geometry of the experimental volumes shown in fig. 3.9, the ^{3}He-distribution becomes

(a) cylindrical volume, radius R=19mm, steel thickness 0.8mm, field of view height h=55mm

(b) rectangular volume, width 28mm, steel thickness 0.2mm, field of view height h=60mm

Figure 3.9: Pictures of the two different experimental volumes

a one-dimensional problem: it varies only along the z-axis (vertical axis). For the cylindrical volume, a geometrical correction $d = 2\sqrt{R^2 - x^2}$ must be made, that means the integrated ^{3}He-concentration must be plotted as function of x, the distance from the center of the experimental volume.

For this geometry, the normalfluid velocity v_n is constant, its potential can thus be written as $\Phi = v_n z$. From equation (3.9) we get:

$$X = C\, e^{v_n z/D} = \frac{X_0\, v_n\, h}{D\,(e^{v_n h/D} - 1)}\, e^{v_n z/D} \tag{3.10}$$

Combined with $v_n = \frac{\dot{Q}}{\rho S T}$ from eq. (3.6) and by taking the logarithm this results in

$$ln(X) = ln(C) + \frac{1}{\rho S T D} \cdot \dot{Q} \cdot z = ln(C) + \frac{\Theta}{D} \cdot \dot{Q} \cdot z \tag{3.11}$$

with $\Theta = \frac{1}{\rho S T}$ as constant for given temperature and pressure. It is calculated from table values, published by R. Donnelly [Do].

For low heating power the liquid can be regarded as isothermal. Then the the logarithm of the ^{3}He-concentration can be plotted as function of z or P. mass diffusion coefficient can be determined directly from the slope of this line, the normalization constant is not important.

Determination of the ^{3}He distribution

The ^{3}He-concentration must be extracted out of the array of gray values recorded by the CCD camera. A model of the setup is shown in figure 3.10. The absorption factors $e^{-\mu l}$ of the different materials commutate, so their order is not important and the calculation can be simplified by changing mathematically the position of the materials, putting first all materials except ^{3}He in the beam.

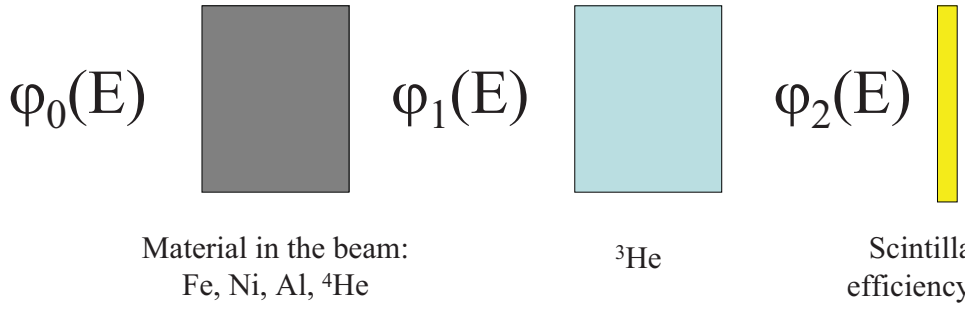

Figure 3.10: Sketch of the setup used to simplify the determination of the ^{3}He distribution.

For a monochromatic neutron beam with wavelength $\lambda = 1.8$Å the calculation would be simple:

$$\varphi_2 = \underbrace{\varphi_0 \cdot e^{-(\mu l)_M}}_{\varphi_1} \cdot e^{-\mu_3 X d} = \varphi_1 \cdot e^{-\mu_3 X d} \tag{3.12}$$

with the subscript M used for any other materials in the beam and μ_3 as total cross section of ^{3}He.

To get the gray value, we need the efficiency of the detector η

$$G = \underbrace{\eta\varphi_0 \cdot e^{-(\mu l)_M}}_{K} \cdot e^{-\mu_3 X d} = K \cdot e^{-\mu_3 X d}. \tag{3.13}$$

With the heater off, the ^{3}He-concentration is uniform ($X^{OFF} = X_0$), it varies only when the heater is switched on. By dividing these two gray values, X can be determined directly:

$$\frac{G^{ON}}{G^{OFF}} = \frac{K \cdot e^{-\mu_3 X^{ON} d}}{K \cdot e^{-\mu_3 X^{OFF} d}} \tag{3.14}$$

$$ln(\frac{G^{ON}}{G^{OFF}}) = -\mu_3 d(X^{ON} - X^{OFF}) = \mu_3 d(X^{OFF} - X^{ON}) \tag{3.15}$$

$$X^{ON} = X^{OFF} - \frac{ln\, G^{ON} - ln\, G^{OFF}}{\mu_3 d} \tag{3.16}$$

Unfortunately the beam is not monochromatic but consists of a wide spectrum, and the gray value is a result of integration:

$$G = \int \eta(E)\varphi_2(E)dE \tag{3.17}$$

$$\frac{G^{ON}}{G^{OFF}} = \frac{\int dE\, \eta\, \varphi_1\, e^{-\mu_3 X^{ON} d}}{\int dE\, \eta\, \varphi_1\, e^{-\mu_3 X^{OFF} d}} \tag{3.18}$$

A division as in equation 3.14 can not be done. The integral could be calculated, but the efficiency of the scintillator is not well known due to irregularities in the ^{6}Li-content and could be measured only for neutrons with $\lambda > 2.7$Å (see page 34).

If the beam is regarded as monochromatic, instead, quantification problems arise because of an effect called *beam hardening*: The distribution of the neutron beam is modified by any material it is passing through. Faster neutrons preferably pass the setup because of their lower cross section, leading to a modification in the neutron spectrum and to changements in the integrated detector efficiency. A detailed discussion and quantification of this effect is made with experimental data in section 3.3.3.

Optimization of the parameters

For an ideal measurement, there should be almost no material in the beam, enough neutron flux for sufficiently good statistics, no heating from neutrons and γ-rays, SVP pressure, a high thermal conductivity in the Helium-mixture and almost no vapour volume. This is obviously not possible, so the parameters must be optimized following the subsequent restrictions:

- **Statistical error:** The objective in our experiment is the determination of a changement of the ^{3}He-distribution in the order of 1%. N_0 is neutron flux, N_1 and N_2 the number of neutrons passing the sample with and without changements in the ^{3}He distribution.

$$N_1 = N_0 \cdot e^{\Sigma_R} \cdot e^{\Sigma_S} \cdot t = N_0 \cdot R \cdot e^{\Sigma_S} \cdot t \tag{3.19}$$

$$N_2 = N_0 \cdot e^{\Sigma_R} \cdot t = N_0 \cdot R \cdot t \tag{3.20}$$

with $\Sigma = \mu l$, the subscript S for the changement in ^{3}He concentration (the signal to resolve), the subscript R and the symbol R stand for any other material. The signal can be extracted with the following equation:

$$\Sigma_S = ln\left(\frac{N_1}{N_2}\right) \tag{3.21}$$

and the error comes from the statistical error of N_1 and N_2. For a small signal the approximation

$$\Delta N_1 \approx \Delta N_2 = \sqrt{R\, N_0 \cdot t} \tag{3.22}$$

The statistical error can so be calculated by solving

$$\Delta\Sigma_S = \sqrt{\frac{2}{R\, N_0 \cdot t}}. \tag{3.23}$$

This is done in figure 3.11 for the cylindrical experimental volume and a ^{3}He concentration $X = 900ppm$. For this calculation, The signal of 1% change in ^{3}He concentration can so be determined with an exposure time of less than 200s.

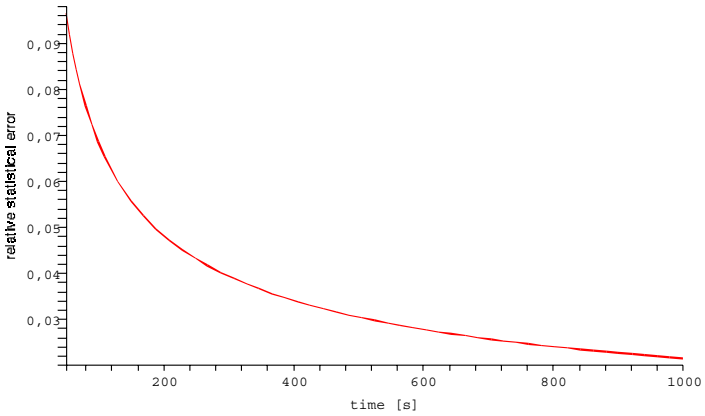

Figure 3.11: Statistical error for a signal of 1% change in ^{3}He concentration $X = 900ppm$.

This excellent statistics is the major advantage to use Neutron Radiography, instead of using a collimated neutron beam and the detection of scintillation light (as used in [La02]).

- **Contrast vs. low thermal conductivity and neutron heating:** To achieve the optimal working point in our apparatus, we would need a ^{3}He-concentration in the order

of $X \sim 10^{-3}$. Unfortunately higher contrast comes with neutron heating: every neutron-^{3}He-reaction (eq. 3.1) produces an energy of 784 keV, the heating power for our different experimental volumes and mixtures is listed in table 3.2.

^{3}He-concentration	Heating power P_N [mW]	
X	cylindrical vol.	rectangular vol.
5.00E-05	0.022	0.019
1.00E-04	0.026	0.022
9.03E-04	0.076	0.067
3.00E-03	0.142	0.135

Table 3.2: Heating power introduced into the experimental volume by neutron absorption

For concentrations $X > 10^{-3}$, the neutron heating power becomes comparable to the induced heating power. For temperatures above 0.8K, where the thermal conductivity of the helium mixture becomes minimal (see fig. 3.1) it can additionally cause a gradient in the ^{3}He-concentration. A possibility to diminish the heating effect would be to scan the experimental volume. This, however, needs more time than is gained by the increased contrast of the higher ^{3}He concentration. To quantify the neutron heating, a scan with a small aperture of the beam limiter for a critical temperature and concentration can be made and compared to the full-size image.

The heating through γ-rays can be neglected for this setup, since in the ANTARES beam are four neutrons per Gamma, and a typical γ photon deposes only some keV through Compton scattering.

- **Thermal inequalities vs. wide range of heating power:** Density, Entropy, thermal conductivity and diffusion coefficient depend on the temperature, and in some cases only poor data is available for helium-mixtures. For the calculations made in eq. (3.6) to (3.11) it is necessary for the liquid to be isothermal, that means the temperature difference between bottom and top of the experimental volume becomes the uncertainty in temperature, therefore it should be limited to 20mK. As can be seen in figure 3.8, the thermal conductivity is especially low in the temperature range from $0.7K$ to $1.6K$. Below and above these temperatures the heating power is limited by the cooling power of the cryostat, estimated to be 3mW-5mW at this temperature.

The Kapitza resistance (a thermal-boundary resistance) can be neglected for this measurement, it has been estimated to be smaller than 1mK (at 1K and 1mW heating power).

- **Scattered neutrons vs. spatial resolution** To achieve a good spatial resolution, the scintillator should be as close as possible to the scintillator. The minimal distance is 12cm, since the outer diameter of the cryostat is 20cm. With this setup, a spatial resolution of about 0.25mm at L/D=400 can be achieved, but around 7% of the signal comes from the light of undesired scattered neutrons. Since the scattered neutron intensity decreases with the distance ($\propto d^{-2}$)) and the fraction of the signal from scattered neutrons should be less than 1%, a distance of 40cm was chosen. Then, the spatial resolution then decreases to 1mm, but this poses no problems to our experiment.

- **Minimization of the vapour volume, measurement at SVP:** As stated on page 24, a vapour volume changes the ^{3}He-concentration in the liquid, especially for temperatures $T > 1K$. The HEVAC-effect must also be considered: the evaporation from the liquid surface and the recondensation at a heat sink makes the He-vapour a very good thermal conductor compared to the liquid [Ha04]. For our geometry this effect is of minor importance, because all the heat flux must pass any vapour at the top of the experimental volume.

  To make the experiment comparable, especially to the precise data from Meyer and Murphy above 1.4K [Mu97], the measurements should be made at saturated vapour pressure (SVP). Since the SVP depends strongly on the temperature, it must be ensured that the transition from liquid to gas (in the capillary) is at the same temperature than the liquid Helium. This is realized by winding a copper capillary around the holder of the experimental volume (see figure 3.12).

- **Minimization of heating power and ^{3}He-concentration** For the neutron EDM experiments and for theoretical reasons, it is desired to work with the lowest ^{3}He-concentration and heating power possible. As mentioned above (table 3.2) the minimal heating power is limited by the neutron heating, the minimal ^{3}He-concentration is limited by the total cross section of ^{4}He. Since a contrast for a difference in ^{3}He-concentration must be achieved, but only the total absorption of the mixture is measured, the measurement with neutron radiography has a limit where the total cross sections of the two components become comparable. The two total cross sections are equal for a ^{3}He-concentration of $X = 2.4 \cdot 10^{-4}$ (see table 3.1). Measurements for $X < 10^{-4}$ are therefore subjected to a bigger statistical error, because the signal of ^{3}He becomes then small compared to the (undesired) absorption of ^{4}He and other materials in the neutron beam.

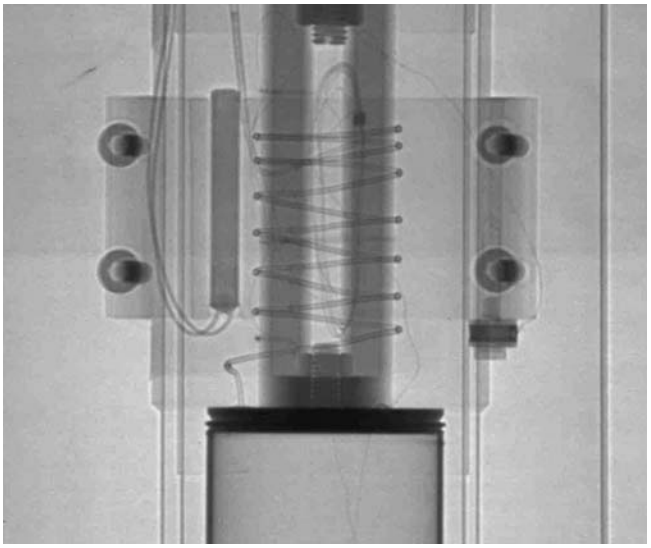

Figure 3.12: Neutron radiography of the holder with winded capillary

3.3.3 Results

Efficiency of the scintillator

To calculate the effects of beam hardening, the efficiency of the used scintillator as function of neutron energy is needed. We used a scintillator from PSI with 300 μm thickness, mounted on a 1.5mm thick Al-plate. It contains $60mg\,cm^{-2}$ LiF, with a ratio $^6Li/Li > 0.9$.
The beam was monochromized with a bicrystal monochromator with a minimal wavelength of 2.7Å. We measured the transmission through the scintillator, corrected for the aluminium ($\sim$ 2%-correction) , as function of the wavelength, for 2.7Å $< \lambda <$ 5.0Å(fig. 3.13). Because of the almost exact 1/v-dependence of the cross section of ^{6}Li, a linear extrapolation on the logarithmic scale can be made [KAE].
With the approximation that all neutrons absorbed by the scintillator are captured by ^{6}Li, the efficiency of the scintillator can be written as

$$\eta = (1 - e^{-(K+\mu'\,\lambda)}) \tag{3.24}$$

with $K = 0.22 \pm 0.04$ and $\mu' = 0.12\text{Å}^{-1} \pm 0.01\text{Å}^{-1}$.

The value K should be compatible with zero, when the absorption of the binding agents is really neglectable. The value of $K = 0.22$ indicates that our approximation does not work well for fast neutrons. However, the composition of the scintillator is not available to us and hence no better approximation is possible.

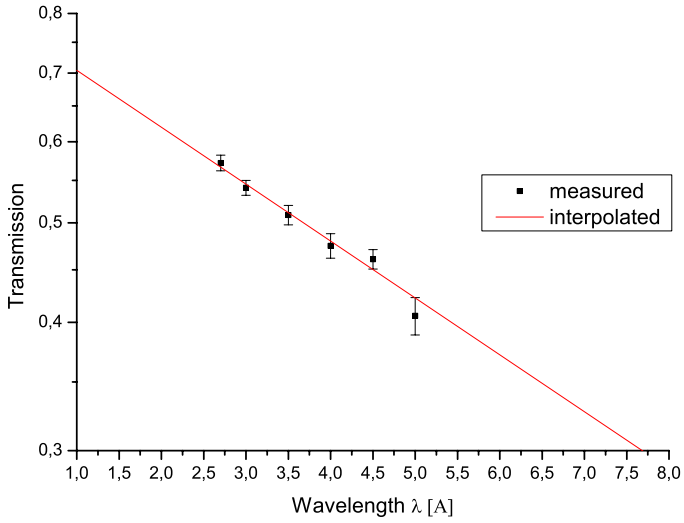

Figure 3.13: Transmission through a $300\mu m$ thick scintillator from PSI, as function of neutron wavelength

Start of the experiment

It turned out to be more convenient to start with the condensation of pure ^{4}He at 3.8K-4K, where the experimental volume can be connected through exchange gas to the CCR-1 cooler with higher cooling power. Even so, the condensation process took 26h, several times the pressure had to be increased to maintain the desired condensation velocity, up to 2 bar. A picture after 6h of condensation can be seen in figure 3.14.

After the condensation process, the exchange gas was pumped so that the experimental volume was thermally isolated from the CCR-1. Then the ^{3}He pot started cooling further through Joule-Thomson expansion, but only with a low cooling power ($\sim$3mW). Then a cold leak with a leak rate of $10^{-5} mbar\, l^{-1} s^{-1}$ was discovered, it connected the experimental volume thermally to the vacuum can at 3.8K. Therefore no cooling below 3.3K was possible and the experiment had to be stopped. A continuation is planned, possible improvements are discussed in section 3.5

Correction for beam hardening

In this section, the beam hardening effect is explained and a precise experimental correction is presented. Figure 3.15 illustrates the calculated modification made in the neutron beam

Figure 3.14: Neutron Radiography of experimental volume during condensation. Exposure time 30s, L/D=800. The ^{4}He is clearly visible in the cell through the scattering cross section. At the bottom of the cell, the heater and the Lakeshore thermometer, both screwed

spectrum by ^{3}He.

When the beam hardening is neglected, severe problems in quantification arise. Then, the beam is regarded as a fictious beam without beam hardening. The differences were calculated and are showed in figure 3.16. For a higher ^{3}He concentration, the beam is more hardened, so it becomes less sensitive to further attenuation and the efficiency of the detector lowers. These two effects add up and lead to a strong overestimation of the ^{3}He concentration when it is calculated from the gray values. For example, a ^{3}He concentration difference of ΔX=900ppm is seen as ΔX=1710ppm (when the beam hardening is neglected), that is an effect of almost 100%.

Beam hardening is the most important error source in this experiment. It can be calculated, however, because spectrum and all the materials in the beam are known. The calculations ca be made with a program developed by Hassanein R.: QNI Quantitative Neutron Imaging [Ha06]. This program is capable to create MCNP input files for different setups, the spectra of different sources and the efficiency of different scintillators are already included in its database.

When the beam hardening is calculated, some data as the efficiency of the scintillator is not

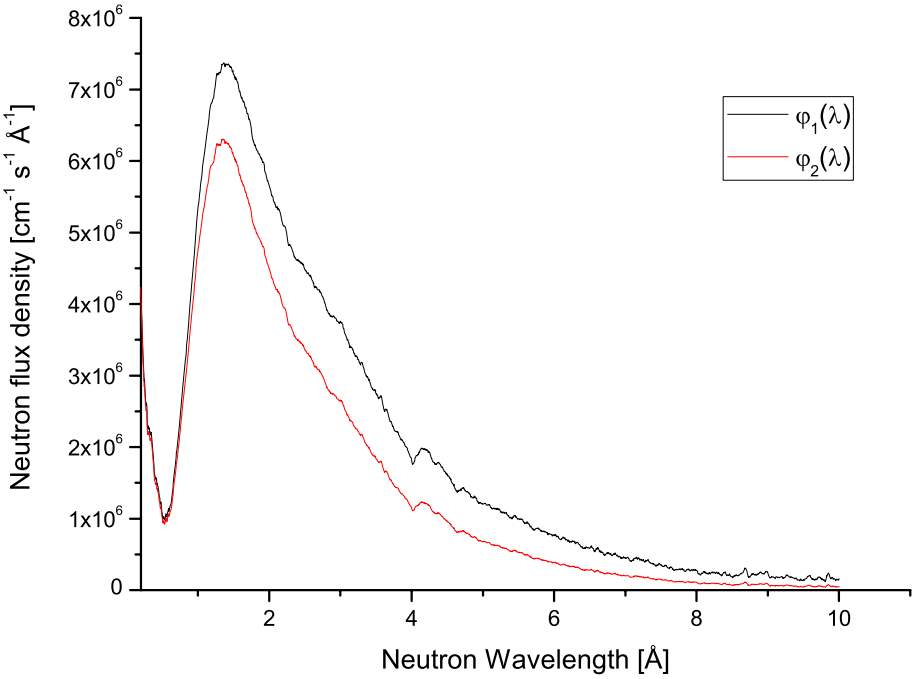

Figure 3.15: Beam hardening effect generated by ^{3}He, exemplary for the center of the cylindrical volume, X=900ppm. φ_1 and φ_2 have been explained in fig. 3.10

known exactly, in our measurement (page 34) the error is bigger than 10%. For the cylindrical geometry, however, a more precise correction through experimental data is possible: The polychromatic case (eq. 3.18) can be handled as monochromatic (eq. 3.15) if the attenuation coefficient is substituted with a concentration dependent attenuation coefficient:

$$\mu_{eff} = \mu_{eff}(X, X_0) \tag{3.25}$$

It follows

$$ln(\frac{G^{ON}}{G^{OFF}}) = -\mu_{eff} \cdot d(X^{OFF} - X^{ON}) \tag{3.26}$$

with μ_{eff} to be determined experimentally. This can be done with a plot of d against $\Sigma_{eff} = \mu_{eff}(d)\ d$. The dependance of μ_{eff} from d is equivalent to a dependance from X, because both values commutate in the exponent. In this work, only a plot for ^{4}He can be presented, because no ^{3}He could be condensed. For ^{4}He the beam hardening effects are very small but can already be seen in fig. 3.17. For ^{3}He, however, the effect is more distinct, a calculation is shown as green line in the figure. To make the two data sets comparable, the ^{3}He

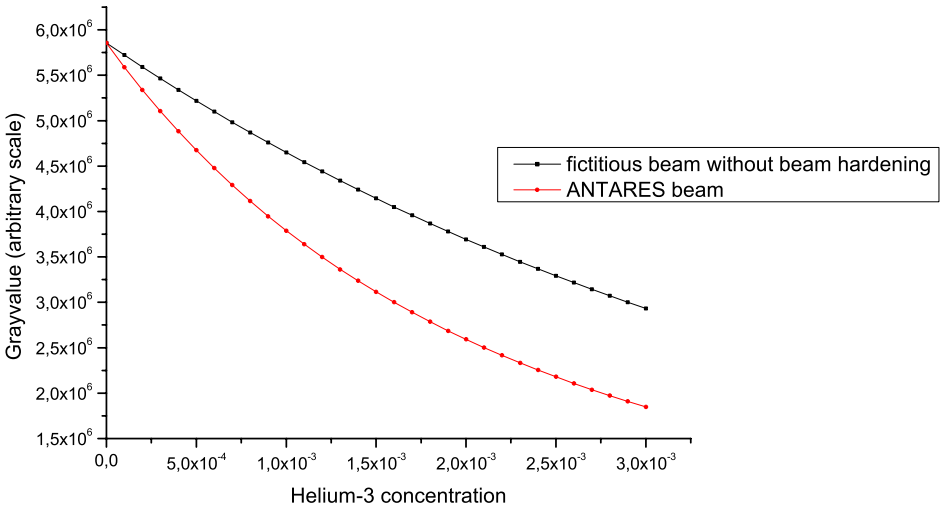

Figure 3.16: Comparison of the gray values measured with the ANTARES beam to a fictious beam without beam hardening. The difference is bigger for a higher ^{3}He concentration

data has been normalized to the ^{4}He data, since the attenuation of X=900ppm ^{3}He is higher than the attenuation of pure ^{4}He.

Using the fictious beam without beam hardening, in fig. 3.17 a line would appear (blue line). With beam hardening effects the curve flattens for higher d, hence a polynomial fit must be made. It is a second-order polynom. For this polynomial fit good statistics are available and all the beam hardening effects are included. The error then depends only on the error of the fitting parameters, which are less than 1% in the example with 30s exposure. For the final measurement the exposure will be much longer, which even lowers the error. This is a big advantage to a calculated correction, where the scintillator efficiency is a lower threshold for the error.

The uncertainty of the fit in figure 3.17 is not solely determined by the statistical error of the data. For every path length d, two values are available, one for each half of the experimental volume. These values oscillate and give the lower error threshold for this correction. The reason for this oscillation could be detector or beam inhomogenities or effects from the beam hardening of the other material in the beam and cannot be given here. The effects, however, could be quantified by measuring the beam hardening effect for samples with well-known size and composition.

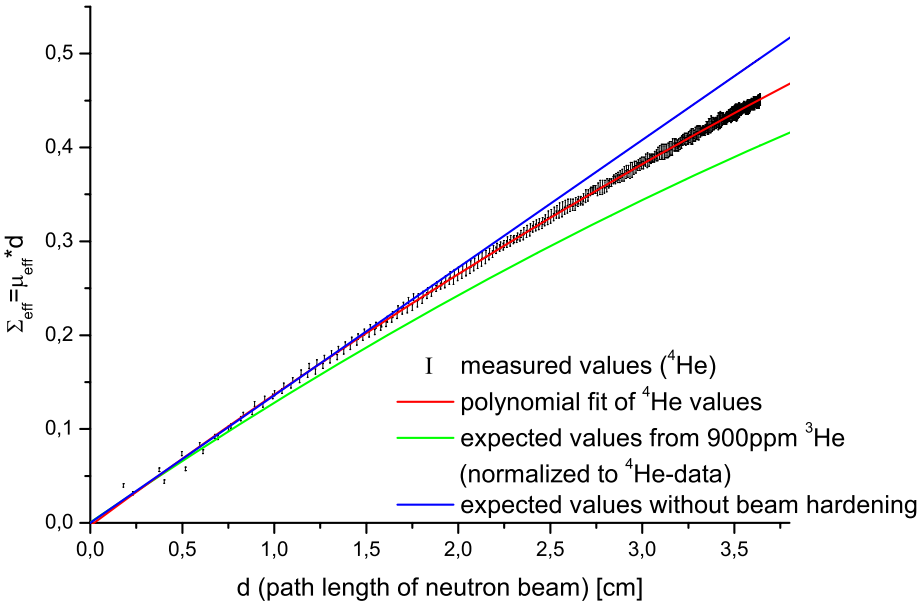

Figure 3.17: Geometrical correction used for a determination of the beam hardening effect (the error bars are represented as the length of the data point lines). The blue line shows the expected behaviour without consideration of the beam hardening, the green line is the expected beam hardening of a X=900ppm ^{3}He concentration. For a better comparison this line has been normalized to the ^{4}He data

3.4 Phase separation of He3-He4-mixtures

For ^{3}He concentrations between 6% to 100% no stable mixture of the two Helium isotopes below the lambda-line (see figure 3.18)exists. When the lambda-line is passed, phase separation occurs. This process could be visualized by performing a dynamic neutron radiography. Depending on the intensity of the neutron beam, a recording speed from 5fps (ANTARES) to 30fps (NEUTROGRAPH) could be achieved.

3.4.1 Theory

Below the lambda point of the He-mixtures phase diagram, shown in fig. 3.18, phase separation occurs.

Below this coexistence curve, also called miscibility gap, two phases, one rich and one poor in ^{3}He, are separated by gravity. The ^{3}He concentration in the ^{4}He-rich phase can be approximated as

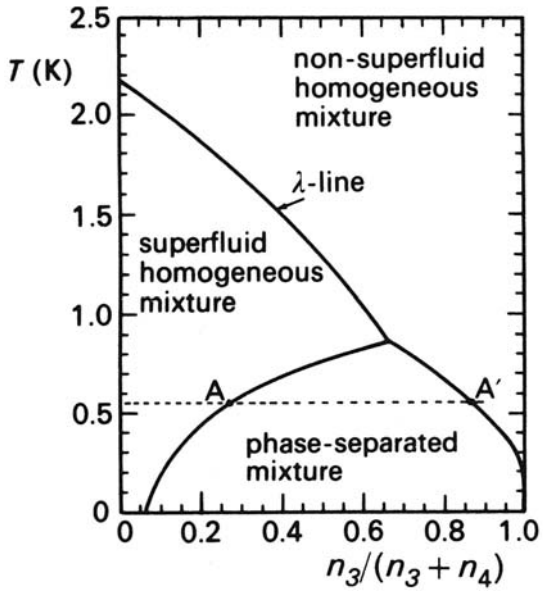

Figure 3.18: Phase diagram of liquid ^{3}He-^{4}He-mixtures

$$X = X_{T=0} \cdot (1 + aT^2 + bT^3). \tag{3.27}$$

with $a = 8.4K^{-2}$, $b = 9.4K^{-3}$ and $X_{T=0} = 0.0648$ the ^{3}He-concentration at $T = 0K$. The ^{4}He concentration in the ^{3}He-rich phase is given by

$$X_4 = c\sqrt{T^3}\, e^{-d/T} \tag{3.28}$$

being $c = 0.85K^{-3/2}$ and $b = 0.56K$ [En00].

When the λ-line is crossed, a first-order phase transition occurs. The ^{3}He-^{4}He-mixtures are an ideal system to study phase transitions and critical behaviour: the superfluid mixture has virtually no impurities, the temperature can be controlled precisely and temperature changes are propagated fast with the second sound. Moreover, extensive measurements on both ^{3}He and ^{4}He have been done and a lot of theoretical work on the phase separation kinetics exist [Ho86].
Disadvantages are the low phase separation temperature, and the rapid decomposition speed, estimated to be in the order of a few seconds and correlated to the diffusion coefficient [Bu94].

When the phase separation occurs, a point inside the miscibility gap transforms to two points (=phases) on the coexistence curve at the same temperature (the points A and A' in figure

3.18). Small droplets of the minority phase[1] form inside the majority phase. Droplets larger than a critical radius R_C grow, but droplets smaller than R_C shrink. Burmistrov et al. estimate the critical radius to be in the oder of 10Å [Bu00]. Assuming homogeneous nucleation, Hoffer et al. estimate the droplet size between 15-23 μm [Ho80]. In contrast, during a heterogeneous separation process, quantized vortices can form and lead to a turbulent demixing process [Pa05]. This could be observed as fluctuations of the ^{3}He concentration during the separation.

Experimentally the kinetics of the phase separation have not yet been clarified. As shown above, ambiguous results have been obtained, it has not been clarified if a heterogeneous or a homogeneous separation occurs. This serves as strong motivation to visualize this first-order transition.

3.4.2 Experimental technique

The easiest way to study the dynamics of phase transition is a sudden parameter change. In our case, the sudden change of the pressure causes the crossing of the coexistence curve.

Creation of the phase transition

Experimentally it is difficult to create a sudden phase transition, Tanaka et al. developed a pressure-sweep method, where a supersaturated state is created through a super leak and pressure variations [Ta02]. Such a supersaturated state however is not stable when neutrons pass the experimental volume. The energy deposit of neutrons and γ-rays creates condensation nuclei and the separation starts immediately. This has been observed in the preliminary experiment at NEUTROGRAPH, described on page 19. That means, for our setup it is essential that the phase transition occurs while the neutron beam is open.

A possible solution follows from pressure dependence of the coexistence curve. When a small pressure ($\sim$ 5 bar) is applied, the position of the curve varies up to 0.1K in temperature (fig. 3.19). When the pressure is released, a sudden phase transition occurs. This method has already been used by Hoffer et al. to observe the phase separation with light scattering [Ho80]. As can be seen in fig. 3.20, the phase diagram is very sensitive on changes in the applied pressure. Hence the quickness of the sudden parameter change is only limited by the velocities

1 The minority phase in the ^{3}He-^{4}He-mixture is ^{3}He for the phase separation from the superfluid mixture and ^{4}He for the separation from the normalfluid mixture. The situation close to the tricritical point is more complicated and is not discussed here

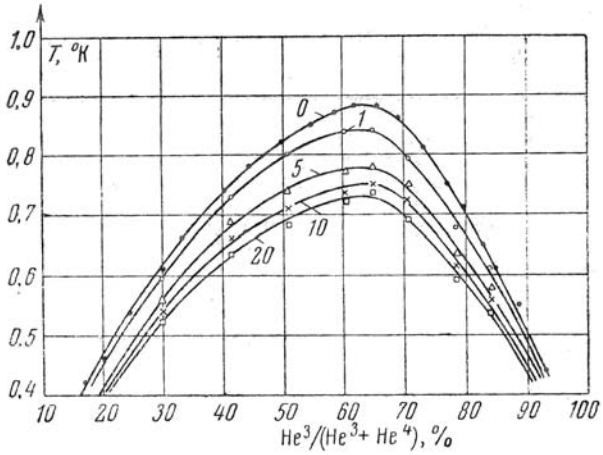

Figure 3.19: Coexistence curve as function of different pressures. Numbers on curves indicate the pressure in atm [Zi63]

in the capillary.

Experimental volume

Only a very thin experimental volume (in the direction of the neutron beam, the Y-direction) is feasible because of the high absorption cross section of ^{3}He. Depending on the spectrum of the neutron beam and the ^{3}He-concentration, a thickness of 0.2mm - 0.5mm would produce the best contrast. For ANTARES, this is 0.2mm for the phase separation of the normalfluid mixture, 0.3mm for the transition from the superfluid mixtures. For NEUTROGRAPH, the corresponding thickness would be 0.3mm or 0.5mm, respectively.

The material with the best properties for this experimental volume is Aluminium, due to its low neutron cross section and the good thermal conductivity. To withstand a pressure of around 10 bar, a wall thickness of 4mm is needed. Figure 3.21 shows an experimental volume out of aluminium (aw-6060) before welding. The dimensions in X- and Z-direction are maximized according to the space inside the cryostat.

Setup

The Setup for this experiment is in principle the same than the one used for the measurement of the mass diffusion coefficient (section 3.3). But due to the high ^{3}He-concentration only a thin experimental volume is feasible. This comes with the advantage to have better contrast,

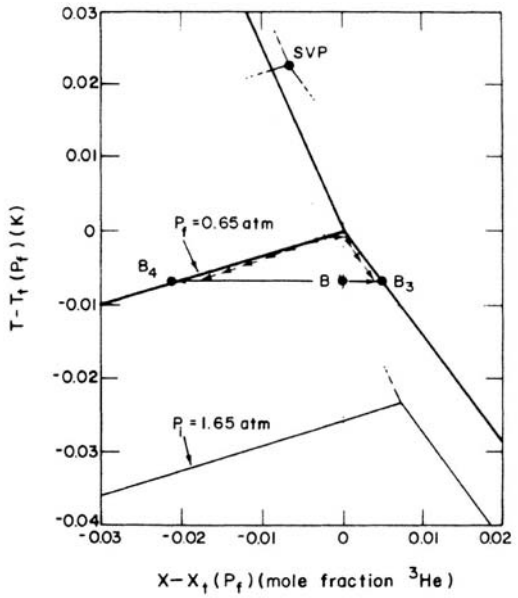

Figure 3.20: Phase diagram and idealized decomposition path for a pressure-induced quench in a ^{3}He-^{4}He mixture (figure based on [Ho86]): When the pressure is changed from $P_i = 1.65\,atm$ to $P_f = 0.65\,atm$ the homogeneous mixture B decomposes into two phases: B_3 and B_4

possibly turbulences in the liquid during the separation process could be observed.

The experimental volume (page 42) must be connected through a wide capillary to the Swagelok system. A fast valve must allow to reduce the pressure from 5bar to 1bar in less then one second. For recording, the ANDOR DV 885 EMCCD camera can be used. It has a fast readout rate of 10^6 pixels/sec., so the exposure time can be maximized. For this CCD-camera, a frame rate of 50fps is easily achievable for our spatial resolution, so the neutron statistics are the limiting factor. This limits the recording speed to 5fps (ANTARES) or 30fps (NEUTROGRAPH).

3.5 Possible improvements for the next experiment

In this section the design of future experimental volumes and modifications in the setup are described.

3.5.1 Setup

In this section, an improved setup without the restriction to use pre-mixed gas mixtures is described.

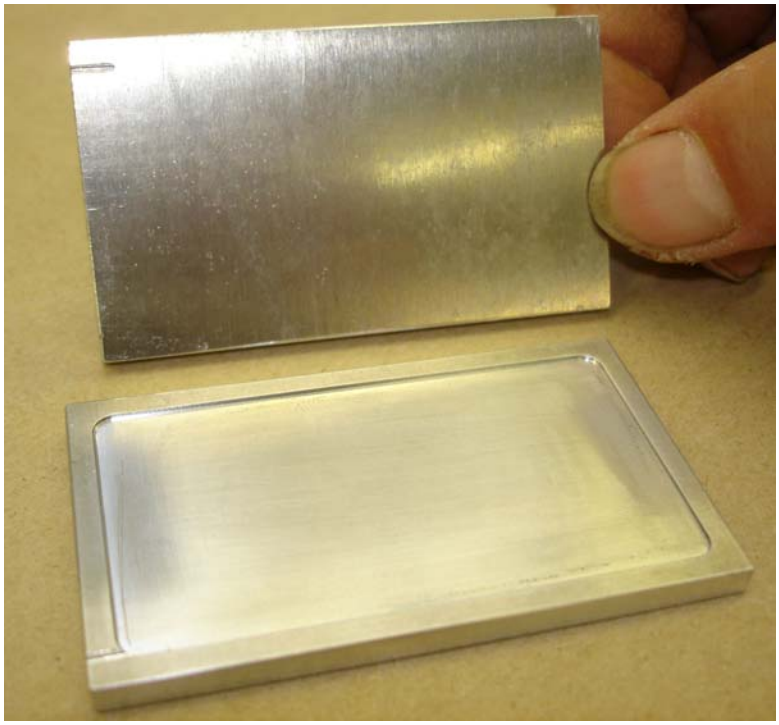

Figure 3.21: Rectangular experimental volume (inner size: 60mm x 32mm x 0.2mm, material: Al aw-6060)

The gas system should be placed on a mounting plate to which the ^{3}He and ^{4}He bottles are connected permanently. High precision pressure gauges (mbar-precision) or precise flow meters can be used to determine the condensed gas and so the ^{3}He-concentration in the mixture. This leads to the advantage that the gas can be mixed during the experiment and the ^{4}He can be condensed in at the higher cooling power of the CCR-1.
The volume of the system must be minimized using capillaries as tubes. Several connections for a vacuum pump must be added to evacuate the parts of the system separately.
To avoid a condensation of the humidity inside a capillary, a cooling trap, which extracts humitidy from the helium, should be added to the gas system. At the end, the gas flow should be regulated through a needle valve with reproducible scale.

The Cryostat could be further modified, adding a heat exchanger to the 50K and 4K levels, to accelerate the condensation. A pressure relief valve should be connected as close as possible to the experimental volume in the case that the experimental volume suddenly heats up.
All outlets of the system must be connected to an exhaust pipe to avoid the contamination of the experimental hall with tritium.

3.5.2 Experimental volume

For all future cells, soldering or adhesive bonding should be avoided. If welding is necessary, only laser beam welding is a reliable method. But even this method can cause leaks, especially when different materials are welded together, as happened in our experiment with copper and steel. The most reliable method is screwing with an indium seal, but it allows only a smaller experimental volume.

At every experimental volume, a test flange should be available to connect it to different cryostats for testing. It should be as small as possible, for example with four M2 screws and a 1mm o.d. capillary.

To avoid any damage for the cryostat if a capillary is blocked (e.g. by ice), a predetermined breaking point must be added to one part of the experimental volume. It can be realized for example in form of a copper membrane, visualized in figure 3.22. In case of an unwanted heat up, the experimental volume breaks at this membrane and the cell can be emptied through the large opening of the vacuum can. The thickness of the membrane should be tested to an opening pressure of 10-15 bar.

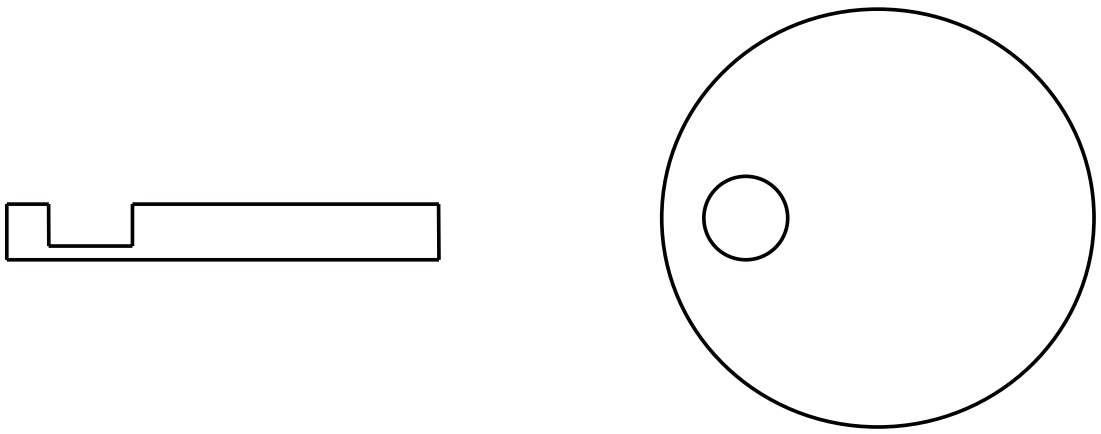

Figure 3.22: Cut through the copper lid (left) and top view (right). The membrane acts as predetermined breaking point

The heater should be connected very well to the bottom of the experimental volume, a standard resistance can be used, but a heating foil (e.g. from MINCO) may be easier to handle. Tests with a cell completely filled with superfluid ^{4}He should be made to quantify the overheating of the bottom as function of the induced heating power.

4. Measurements on aluminium alloys 7449

In a previous experiment at NEUTROGRAPH, a correlation between the Vickers hardness and the attenuation coefficient in an AA7449 Al-Mg-Zn alloy has been found [Ba06b]. The following experiment tries elucidate further the reasons for the variation of the total neutron cross section in this material. It was performed in collaboration with Axel Steuwer and Jens Altenkirch from FAME38 at ILL.

4.1 Theory: Hardening of Aluminium Alloys

Pure aluminium does not have the required hardness for many applications, especially for the aerospace structural applications. Hence many aluminium alloys are strengthened by age hardening to improve their mechanical properties. Age hardening is a form of heat treatment (temperatures generally 120°C-180°C), where the hardness of the alloy increases. When no heat is applied (room temperature), the ageing process is called natural ageing.

This section is focused on precipitation, only one age hardening mechanism in alloys. When an aluminium alloy hardens, precipitates of the minority materials in the aluminium are formed. Generally, they can be considered as obstacles which hinder the motion of dislocations and harden the material [Po95].

Here, the precipitation hardening is explained for Al-Cu alloys (2xxx series) because it is a relatively simple alloy. The precipitation processes in the 7xxx series, however, are basically the same, but η particles ($MgZn_2$) build instead of copper precipitates.

Before the age hardening can start, the alloy must be solution treated. That is made through a heat-treatment at a temperature, where it exists as α-solid solution (500°C-550°C). After about 20 minutes at this temperature, all precipitations are solved because of the higher solubility of the copper at higher temperatures. Now the age hardening can start (it is explained in the enumeration below, figure 4.1 is the accompanying illustration).

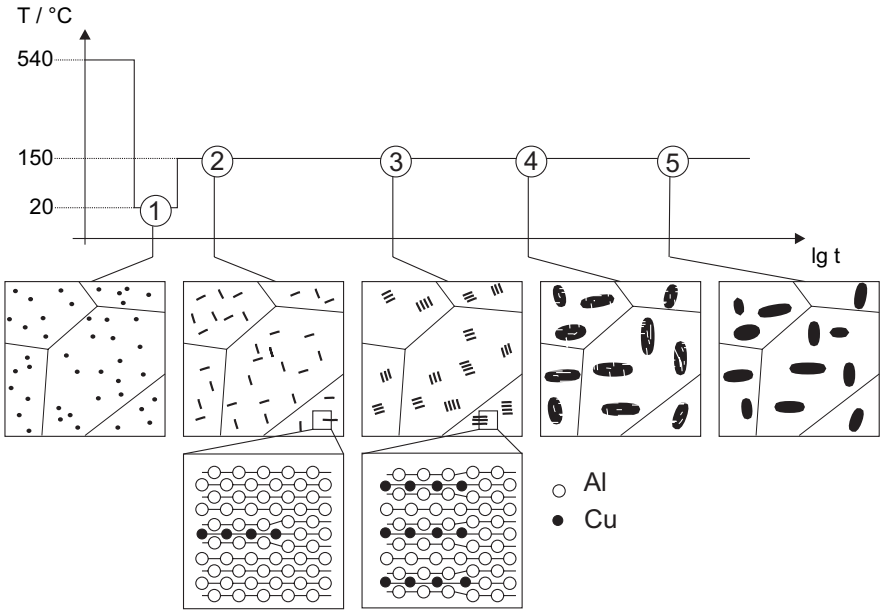

Figure 4.1: Age hardening processes inside an Al-Cu alloy (explained in the text): SSSS (1) → GP zones (2) → Θ″ (3) → Θ′ (4) → Θ (5), from [Ro05]

1. To get a Supersaturated Solid Solution (SSSS), the alloy must be quenched to room temperature (e.g. in water). Now the copper has a lower solubility and Cu precipitation nuclei form inside the aluminium. The number of the precipitation nuclei varies with the degree of supersaturation.

2. The alloy is heated to around 150°C, where Guinier-Preston zones (GP or GP-I) form inside the Al matrix. GP zones are single-atom layers of Cu on the {100} planes of the Al matrix. They can be regarded as fully coherent[1] metastable precipitates. GP zones also grow when the material is naturally aged, but the process is much slower (factor 10-100).

3. Θ″ precipitation[2] is the second rise in hardness: The Θ″ phase is considered as two (or more) layers of copper, separated by aluminium. Θ″ precipitation comes with a change in the lattice structure. Its thickness can be 10nm at a diameter of around 100nm.

4. The Θ′ phase is building. It consists of Cu discs, which have their own crystal structure (thickness ∼30nm). These changements in crystal structure lead eventually to a

1 coherent means that the precipitates have a strict lattice and orientation correspondence with the surrounding matrix

2 Sometimes, the Θ″ precipitations are called GP-II zones

changement in the attenuation coefficient (see section 4.2)

5. The Θ phase is the final, stable phase of the precipitates. When this phase appears, the alloy is already over-aged, that means the hardness is lower than its peak value.

Age hardening is a very complicated process and many effects have not yet been clearly understood. A more detailed description can be found in [Ri00].

4.2 Visualization of Vickers Hardness by Neutron Radiography

Changements in the crystal structure can lead to differences in the neutron scattering cross section, as can be seen in the Bragg edges of different materials (see fig. 4.2). A change in cross section causes a modification of the attenuation coefficient μ (see eq. 2.2). A variation in μ as function of the Vickers hardness[3] has been observed by Ballhausen et al. in a Neutron Tomography of a Friction Stir weld[4].

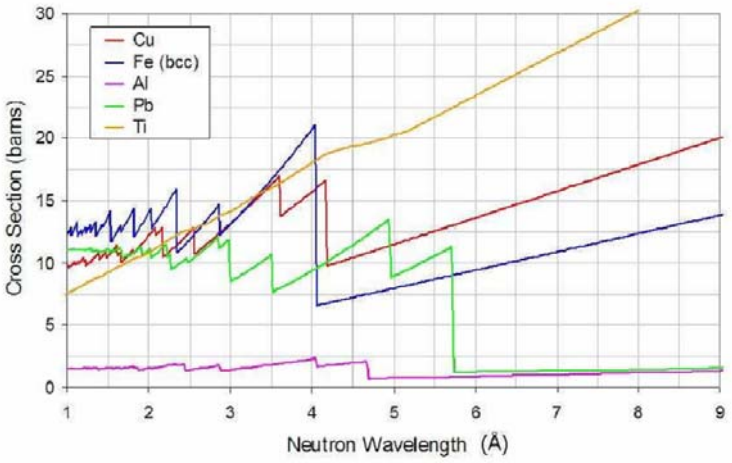

Figure 4.2: Neutron Cross section of different materials as function of wavelength (from [Ch06]). Differences in the neutron cross section occur at distinct wavelengths, they are called Bragg edges

The next step is to determine the reason for the variation of the attenuation coefficient, since many effects can lead to differences in the neutron cross section, including texture effects[5] and

3 The Vickers hardness is a hardness measurement method, where a diamond intender is pressed with well-defined pressure into the material. The hardness is then calculated from the surface area of the resulting indentation.

4 Friction Stir Welding is a joining technique solely based on mechanical fusioning below the melting point. The workpieces are pressed upon each other and a rotating cylindrical tool with a drill on its tip is driven between them (from [Ba06b])

grain structure. Therefore, a radiography of differently aged hardenened aluminium 7449 alloys has been made and the Vickers Hardness has been compared to the attenuation coefficient. For this alloy, precipitation hardening dominates other hardening effects. The obtained data has been compared to the correlation obtained by Ballhausen et al.

4.2.1 Sample preparation, Setup

Two pieces with the size (12mm x 37.5mm x 152mm) were cut out of the same piece of AA7449 Al-Zn-Mg alloy. 8 holes (diam. 1.2mm, depth 6mm, distance 15mm) for the thermocouples were drilled into each sample.

The solution treatment has been performed in a furnace from ESRF. The samples were heated up to 520°C, this temperature was then hold for 25 min. Afterwards, a temperature quenching to 20°C into water was performed. Then, both samples were naturally aged at 23°C for seven days.

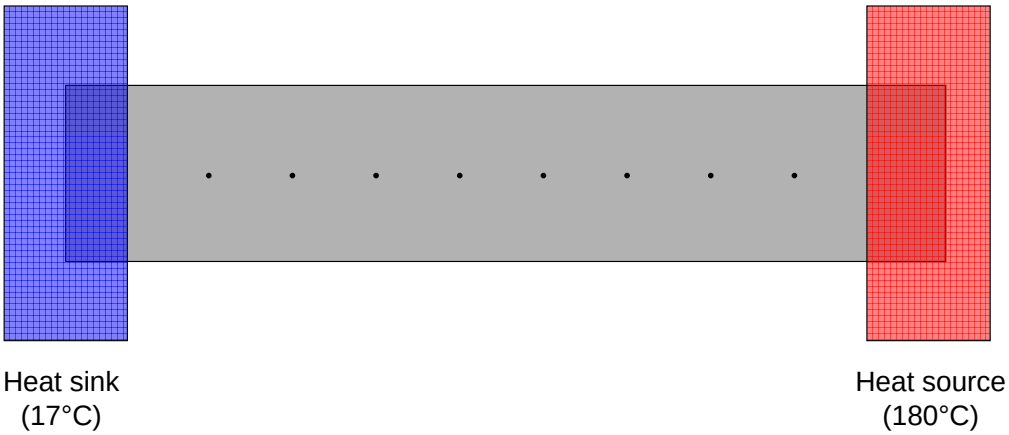

Figure 4.3: Illustration of the apparatus to generate a temperature gradient inside the sample.

Sample 1 was then naturally aged for two more days, while sample 2 was heat treated in an apparatus built to generate a temperature gradient inside the samples. An illustration is shown in figure 4.3. The heat sink and source are fixtures out of aluminium connected to a water

5 Texture is the distribution of crystallographic orientations of a sample. A sample in which these orientations are fully random is said to have no texture. For a sample with texture the neutron cross section varies as fuction of the angle between sample and neutron beam. When the sample is rotated (as done in the tomography of a friction stir weld) this can lead to changements in the reconstructed attenuation coefficient.

cooling system and to two heating elements, respectively.

The hot side was connected to two PTC self-regulating heating elements, fabricated by DBK. They can be directly connected to a 220V/240V 50Hz plug and achieve a temperature of 180°C at a heating power of 180W each. The left cold side was connected through four 6mm copper tubes to the ILL water cooling system, which provides water at 15°C and 7bar. The temperature was surveyed with five Type K thermocouples, fabricated by JDMesure and connected to the National Instruments Multifunction DAQ 6024E with integrated temperature sensor. The temperatures were recorded every ten seconds with a LabView virtual instrument.

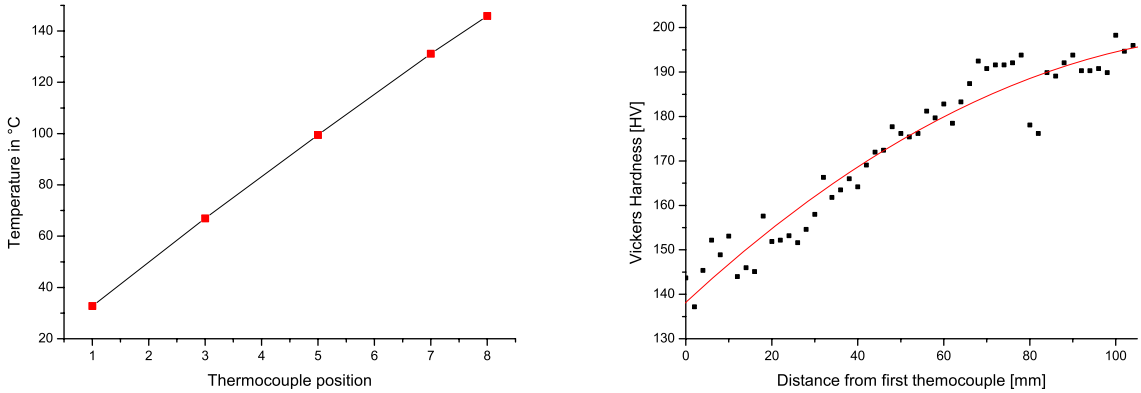

(a) Temperature gradient in the sample during age hardening

(b) Hardness gradient in sample 2 after heat treatment with polynomial fit

Figure 4.4: Heat treatment of sample 2

Ten minutes after having switched on the heating elements, the desired linear temperature gradient was reached (see fig. 4.4a) and was hold for 20 hours. Then, the heating elements were switched off and the sample was cooled to the temperature of the heat sink. A hardness measurement was performed at the same day on a BUEHLER MicroMet 5104 Hardness Tester. The test load range was 1000g, every 1-2mm a point was measured. The result of the measurement of sample 2 can be seen in fig. 4.4b

The next day, a neutron radiography of both samples was performed.

4.2.2 Results

The neutron radiography is a sum of 3750 images with an exposure time of 0.2 seconds. The image series has been corrected with the γ-filter developed by Ballhausen [Ba06], then a dark and an open beam correction was made. The pixels were binned vertically, where the same temperature was applied and so the same Vickers hardness is expected. Then the logarithm was taken to extract the attenuation coefficient. By comparing the radiography to the sample (Pixel size: 156.7 μm) a local attenuation coefficient was assigned to every point on the sample. Then the attenuation coefficient can be correlated with the Vickers hardness.

In fig. 4.5 the attenuation coefficient is compared to the hardness for both samples. No correlation between the Vickers Hardness and the attenuation coefficient could be found. Other effects as the change of gray values caused by scattered neutrons have a much higher impact than the variation of the attenuation coefficient through the precipitations of Mg and Zn in the aluminium alloy.

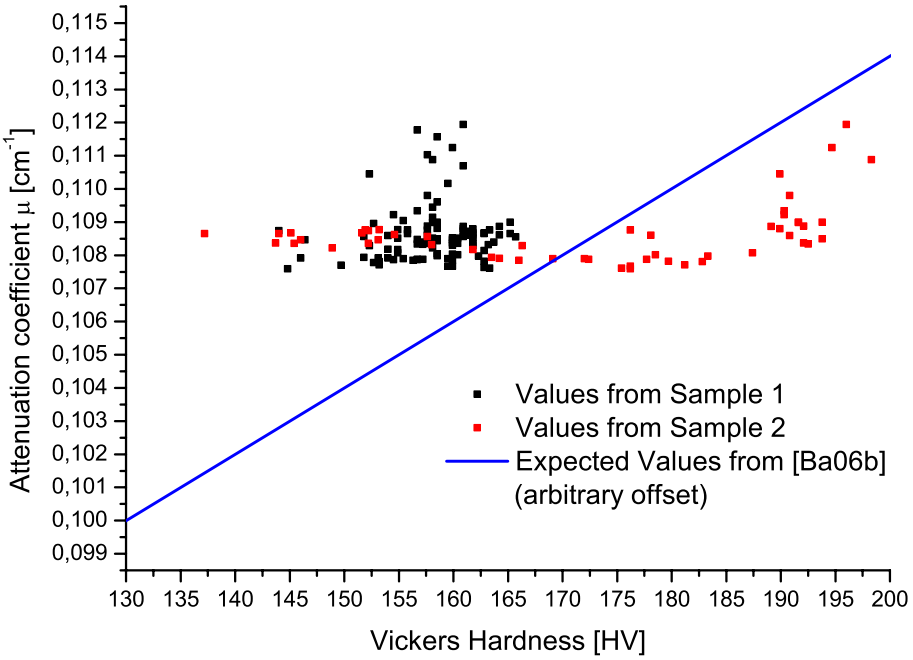

Figure 4.5: Attenuation coefficient, extracted from Neutron radiography gray values is compared to the Vickers Hardness. Sample 1 was naturally aged, sample 2 was heat-treated. The blue line is the correlation found by Ballhausen et al.

The correlation seen by Ballhausen et al. could so not be confirmed. It is possible, though, that texture effects have caused the variation in the attenuation coefficient during the tomography of the friction stir weld. Texture differences and differences in grain structure appear in a friction stir weld due to mechanical forces applied by the cylindrical tool used for welding [Du06].

5. Experiments at Neutrograph in progress

In this chapter, some planned experiments are presented. The dynamical measurement of the TLP bonding process (section 5.1), a time-resolved, stroboscopic measurement of an injection nozzle (section 5.2) and the possibility to investigate water distribution in a running fuel cell (section 5.3).

5.1 TLP Bonding

Transient liquid phase bonding is an advanced bonding technique: a thin foil (typically $50\mu m$ thick) is placed in between two pieces (of the same material). It acts as melting point depressant. The assembly is then heated to the brazing temperature (below the melting point), which varies according to the foil type (800°C-1300°C). At this temperature, the material next to the foil melts and components of the foil start to diffuse. Now, the liquid phase starts to extend outwards. At the end of the process, only small concentration differences of the bonding foil materials should remain.

The TLP bonding process requires typically some hours, with around 15 min at the brazing temperature. More details can be found in [Ba07b], where a neutron radiography of a TLP bond is described. Neutrons are very sensitive to the boron in the foil, but can penetrate the steel easily. The diffusion of the boron can so be observed with high contrast.

The next step would be the dynamic observation of the diffusion process. Inside an oven from the ILL sample environment a TLP bonding assembly can be heated and the diffusion of the boron can be observed dynamically. This experiment has been prepared but could not yet be carried out, a detailed description is made here.

5.1.1 Sample preparation

The available samples are 20 pieces out of 50 B grade steel, with the size 20mm x 20mm x 5mm. To use them in the sample holder (see section 5.1.2), they have to be reduced to 20x15x5mm and their surface must be polished with a maximal roughness of 5 μm, at least on the side where they are bonded. The foil used for bonding is a Metglas MBF-51 brazing foil. It consists of 15.0% Cr, 7.25% Si, 0.06% C, 1.4% B, balanced with Ni [MG]. The recommended brazing temperature is 1195°C. It must be degreased and cut in adequate pieces before use. The samples and the foil were provided by A.J. Smith from the Sheffield Hallam University, UK.

Additional an 1mm-hole for a thermocouple can be drilled into every other sample. Type K thermocouples are available from the Al-hardness experiment (section 4).

5.1.2 Sample environment

To perform the bonding, a sample environment with a vacuum better 10^{-4} mbar or an inert atmosphere is needed, and an oven suitable for temperatures bigger than 1300 °C. At the ILL, the furnace 09TL19AN50 would be the best choice. It is a top loading furnace, with a sample size of (diameter-length) 35mm-50mm, connected to the inset with an M8 threaded stud.

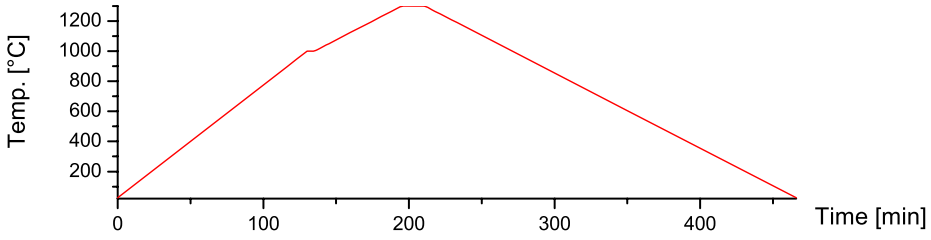

Figure 5.1: Typical heating cycle for a TLP bonding procedure

In fig. 5.1 a typical heating cycle for the bonding process is drawn. It starts from room temperature to 1000°C with a slope of 7.5°C/min, then a dwell for 5 minutes. From 1000°C to 1300°C at 5°C/min and a dwell for 15 minutes. Finally 1300°C to room temperature with a decrease rate of 5°C/min. The maximum temperature varies according to the recommended brazing temperature of the joining foil.

The sample holder for this furnace (fig. 5.2) has been designed in collaboration with S. Hennenberger from the Physics Institute of the University of Heidelberg. The used material is niobium, due to his good high temperature properties and the possibility to erode it. With this sample holder, the bonding assembly can be put into the furnace without the use of a screw. The pieces are simply clipped together. This makes it possible to use it for several bonding procedures. Nevertheless at least two of the sample holder should be machined and tests should be done in advance (section 5.1.3).

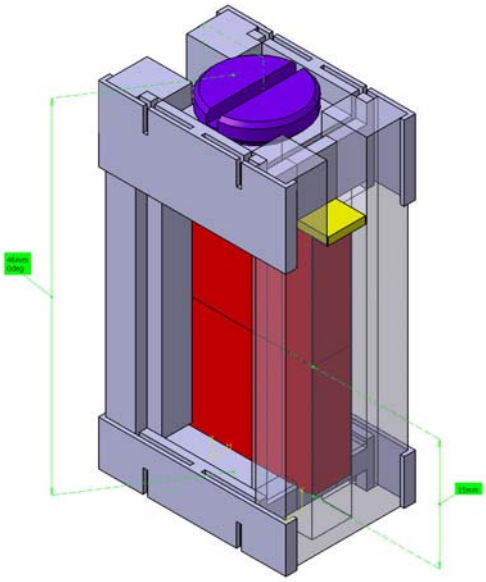

Figure 5.2: Sample holder for a time-resolved radiography of a TLP joining process: the 50B grade steel (red), the connection to the furnace visualized as M8 screw and a niobium foil (yellow) are shown. The bonding foil is not visible in the figure.

The bonding pressure is another important joining condition, the optimum would be a pressure between 1-3MPa on the bonding foil. For adjusting it to this value, a special furnace with online regulation of the pressure would be needed. Such an oven is used for the optimization of the bonding parameters at The Welding Institute, UK, but is not suitable for neutrons. In that furnace the sample is connected through graphite blocks to the outside, where the pressure is applied.

With our setup the bonding pressure can only be varied by inserting small niobium foils (marked yellow in fig. 5.2) between holder and sample. The pressure comes then from the greater thermal expansion of the steel compared to the niobium. With this procedure, a pressure above

the threshold of 1Mpa can be applied, the maximum value, however, is given by the bending strength of the sample holder. Moreover, the niobium foil prevents the contamination of the threaded stud with steel in case of overheating.

5.1.3 Realization

Before performing the experiment inside the beam line furnace, a test experiment with the sample holder inside a normal furnace (e.g. the one from the FAME38 group at ILL) should be made. After a typical heating cycle (fig. 5.1) has been applied, a radiography can be made to examine the success of the procedure. Then the dynamic radiography of the bonding process can be performed.

To observe the bonding process with sufficient spatial resolution, the beam limiter should be used in the pinhole mode (described in section 2.4.2). To achieve a spatial resolution of 0.5mm a L/D ratio of 400 is needed. An 10mm-opening of the beam limiter leads to this value. They result in a neutron flux of $2 \cdot 10^8 n\, cm^{-1}\, s^{-1}$. At the beginning of the heating cycle the boron absorbs around 50% at the place of the foil, hence an exposition time below 1s is possible. After the complete diffusion it absorbs less than 1% of the beam. Then, a longer exposition time is needed (10-30s). Since the diffusion process slows down at the end, a sufficient time resolution is ensured at any time.

5.2 Injection nozzle

The fuel distribution inside and in front of an injection nozzle has not yet been visualized with sufficient resolution in space and time. Imaging with Synchrotron X-Rays was made but did not bring sufficient contrast. At NEUTROGRAPH, stroboscopic images of an injection nozzle were performed and differences compared to the visualization with other methods have been revealed: with optical methods the fuel dust could not be penetrated, so only a cloud of fuel can be seen. The neutron radiography, in contrast, shows a density distribution of the fuel.

An improvement in spatial resolution can be achieved when the injection nozzle is scanned with a pinhole, a method described in [Ba07]. In this setup, the spatial resolution is not limited anymore by the scintillator, but only by the pinhole size, the beam collimation and the distance between pinhole and object. An iris is placed between sample and scintillator. On the scintillator a light spot can be seen, its integrated intensity is proportional to the transmission

through the part of the sample in front of the iris. The NEUTROGRAPH software automatically integrates over this spot and moves the sample. In the final image, every sample position corresponds to one pixel.
Figure 5.3 shows such an image of an injection nozzle used for test reasons, it has not been optimized for spatial resolution. With this setup, a resolution better than 50 μm is easily achievable.

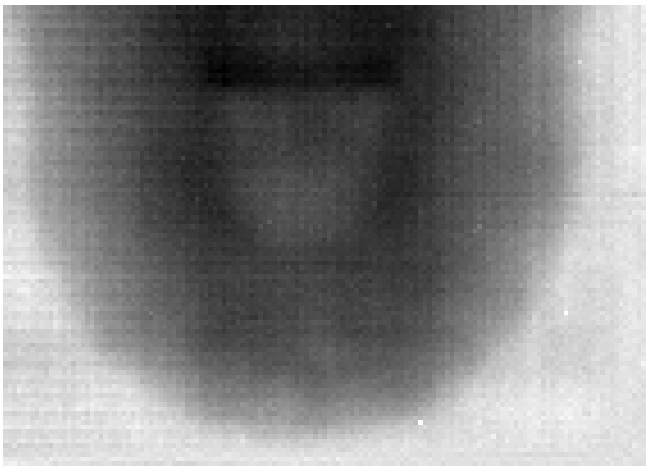

Figure 5.3: The top of an injection nozzle scanned with the pinhole method (described in the text)

A collaboration with an industry partner to investigate the fuel distribution inside and around an injection nozzle is planned in 2008.

5.3 Fuel Cells

There is a great need to understand the water management inside PEFC fuel cells. The water distribution inside a running fuel cell has not yet been measured with sufficient precision. There are different areas where a quantification of the water distribution is needed: The gas diffusion layer (GDL), the microporous layer (ML), the catalyst layer (CL) and the inflow/outflow regions. To investigate the CL and the ML a spatial resolution $< 10\mu m$ is needed, which is not possible with neutron radiography. Sinha et al. compared different techniques for quantifying the water distribution in a fuel cell (table 5.1).

Neutron radiography and tomography is much faster than MRI and much more sensitive to water than X-Ray images. Stationary images of fuel cells have already been made [Kr05] and the feasibility of a dynamic tomography in less than 10s at NEUTROGRAPH has been

	X-ray imaging	Neutron imaging	MRI
Sensitivity to water	Sensitive	Extremely sensitive	Extremely sensitive
Spatial resolution			
Present	10 μm	100-150 μm	25 μm
Future	1 μm	10-50 μm	10 μm
Temporal resolution (for a single image: radiograph or shadowgraph)	0.07 s	0.03 s	50 s
Disadvantages for fuel cell research	✓Less sensitivity to water	✓Complex and costly technique ✓Low spatial resolution prevents its use in MPL and CL	✓Requires absence of magnetically inductive materials, e.g., carbon ✓Unsuitable for CL, MPL and GDL due to the presence of carbon ✓Low spatial and temporal resolution

Table 5.1: Comparison of X-Ray, neutron radiography and MRI as application for imaging of the water distribution of a fuel cell [Si06]

.

demonstrated [Tr07]. A further investigation of PEFC cells is planned in collaboration with the CEA.

Bibliography

[Ab68] Abel W.R., Wheatley J.C.: *Experimental thermal conductivity of two solutions of ^3He in superfluid ^4He*, Phys. Rev. Lett. 21 (1968) 1231

[Al05] Allen P.B., http://felix.physics.sunysb.edu/ allen/540-05/ (2005)

[Ant] Advanced Neutron Tomography and Radiography Experimental System, http://www.physik.tu-muenchen.de/antares

[Al38] Allen J.F., Misener A.D., Nature 141 (1938) 75

[AZOM] Azom - The A to Z of materials, http://www.azom.com

[Ba06] Ballhausen H., Abele H. et al.: *New algorithms for noise reduction and gamma background removal in neutron imaging data*, not published, 2006

[Ba06b] Ballhausen H., Abele H. et al.: *Neutron Tomography of a Friction Stir Weld*, not published, 2006

[Ba07] Ballhausen H., *Methoden und Anwendungen fuer bildgebende Verfahren mit hohen Neutronenfluessen*, PhD Thesis, 2007

[Ba07b] Ballhausen H., Abele H., *Neutron Radiography Analysis of a Transient Liquid Phase Joint*, 2007, arXiv:cond-mat/0604450v1 [cond-mat.mtrl-sci]

[Be52] Beenakker J.J.M., Taconis K.W. et al.: *Heat conduction in Helium II containing some ^3Helium*, Physica 18 (1952) 433

[Bu94] Burmistrov S.N., Dubovskii L.B.: *Growth Kinetics of He3-rich Phase During the Phase-Separation In a Liquid He3-He4-mixture*, Physica B 194-196 (1994) 883

[Bu00] Burmistrov S.N., Chagovets V. et al.: *On the structure of quantized vortices in a saturated liquid 3He-4He mixture*, Physica B 284-288 (2000) 321

[Ca06] Carlson D.: *Three-dimensional imaging of earth and planetary materials*, Earth and Planetary Science Letters 249 (2006) 133-147

[Ch06] Kun Chen: *A STUDY OFSPECTROSCOPIC, COLD NEUTRON RADIOGRAPHY*, PhD Thesis, 2006

[Cl92] McClintock P.V.E., Merendith D.J., Wigmore J.K., *Low-Temperature Physics - An Introduction for Scientists & Engineers*, Blackie & Son Ltd., Glasgow (1992)

[Dau47] Daunt J.G. et al., J. Chem. Phys. 15 (1947) 759

[Do] Donnelly R.J., Barenghi C.F., *The Observed Properties of Liquid Helium at the Saturated Vapor Pressure*, http://www.uoregon.edu/∼rjd/vapor1.htm

[Du06] Dumont M., Steuwer A. et al.: *Microstructure mapping in friction stir welds of 7449 aluminium alloy using SAXS*, Acta Materialia 54 (2006) 4793

[En00] Enss C., Hunklinger S., *Tieftemperatur Physik*, Springer, Berlin (2000)

[Fe03] Ferger T., A*ufbau einer dynamischen Radiographie- und Tomographiestation mit thermis- chen Neutronen*, diploma thesis, Heidelberg University, 2003

[Gi03] Gildemeister A., *Fast dynamic radiography at a high-flux thermal neutron beam*, diploma thesis, Heidelberg University, 2003

[Go94] GOLUB R., LAMOREAUX S.:*NEUTRON ELECTRIC-DIPOLE MOMENT, ULTRACOLD NEUTRONS AND POLARIZED 3HE*, Phys. Rep. 237 (1994) 1

[Ha04] Hayden M.E., Archibald G. et al.: *Neutron-Detected Tomography of Impurity-Seeded Superfluid Helium*, Phys. Rev. Letters 93 (2004) 105302

[Ha06] Hassanein R., *Correction Methods for the Quantitative Evaluation of Thermal Neutron Tomography*, dissertation at the ETH Zurich and the Paul Scherrer Institut, Villigen, Diss. ETH No 16809, http://e-collection.ethbib.ethz.ch/cgi-bin/show.pl?type=diss&nr=16809

[Hi05] Hillenbach A., Engelhardt M. et al.: *High flux neutron imaging for high speed radiography, dynamic tomography and strongly absorbing materials*, Nuclear Instruments & Methods in Physics Research A 542 (2005) 116-122

[Hi06] Hilger A., Kardjilov N. et al.: *The new cold neutron radiography and tomography instrument CONRAD at HMI Berlin*, Physica B 385-386 (2006) 1213-1215

[Ho80] Hoffer J.K., Campbell L.J. et al.: *Observations of Homogeneous Phase Separation in Liquid 3He-4He-mixtures*, Phys. Rev. Lett. 45 (1985) 912

[Ho86] Hoffer J.K., Sinha D.N.: *Dynamics of binary phase separation in liquid 3He-4He-mixtures*, Phys. Rev. A 33 (1986) 1918

[Hu05] Hussey D., Jacobson D. et al.: *New neutron Imaging facility at the NIST*, Nuclear Instruments & Methods in Physics Research A 542 (2005) 9-15

[KAE] Korea Atomic Energy Research Institute, Nuclear Data Evaluation Lab., http://atom.kaeri.re.kr/

[Kr05] Kramer D., Lehmann E. et al.: *An on-line study of fuel cell behavior by thermal neutrons* Nuclear Instruments & Methods in Physics Research A 542 (2005) 52

[La49] Landau L.D., Pomeranchuk I.Ya. et al., Doklady Akad. Nauk SSSR 69 (1949) 165

[La02] Lamoreaux S.K., Archibald G. et al: *Measurement of the 3He mass diffusion coefficient in superfluid 4He over the 0.45-0.95 temperature range*, Europhys. Lett. 58 (2002) 718

[Lo38] London F.: *The λ-phenomenon of liquid helium and the Bose-Einstein degeneracy*, Nature 141 (1938) 643-4

[Lo74] Lounasmaa: *Experimental Principles and Methods Below 1K*, Academic Press Inc., London, p. 31 (1974)

[Le96] Lehmann E., Pleinert H. et al.: *Design of a neutron radiography facility at the spallation source SINQ*, Nuclear Instruments & Methods in Physics Research A 377 (1996) 11-15

[Le07] Lehmann E., Frei G. et al.: *The micro-setup for neutron imaging: A major strp forward to improve the spatial resolution*, Nuclear Instruments & Methods in Physics Research A 576 (2007) 389-396

[MG] Metglas Brazing Foils, http://www.metglas.com/products/page5_1_1_2.htm

[Mu97] Murphy D., Meyer H.: *Heat Transport in Dilute Mixtures of 3He in Superfluid 4He*, J. Low Temp. Phys. 107 (1997) 175

[NDB01] Dianoux A., Lander G. (Editors), Neutron Data Booklet, Institut Laue-Langevin, Grenoble, 2001

[Neut] Neutron Imaging and Activation Group at the Paul Scherrer Institute, http://neutra.web.psi.ch/

[Os04] Oseen-Senda K.M., Lundell F., Hillenbach A., Pauchet J., *Visualisation of Low Heat and Mass Flux Boiling in a Small Metal Pipe Using Neutron Radiography*, Proc. ICMM2004, Rochester (New York), 2004

[Pa05] Pashitskii E.A., Mal'nev V.N. et al.: *Vortex nucleation in the process of phase separation of a supersaturated 3He-4He mixture*, Low Temp. Phys. 31 (2005) 105

[Po95] Polmear I.J.: *Light Alloys: Metallurgy of the Light Metals*, Butterworth-Heinemann (1995)

[Pt61] Ptukha T.P., *Thermal conductivity and diffusion in Weak ^{3}He-^{4}He solutions in the temperature range from the λ point to 0.6 K*, Soviet Phys. JETP 13 (1961) 1112

[Ri00] Ringer S.P., Hono K.: *Microstructural Evolution and Age Hardening in Aluminium Alloys: Atom Probe Field-Ion Microscopy and Transmission Electron Microscopy Studies*, Materials Characterization 44 (2000) 131

[Ro05] Roebel, M.: *Ab-initio-Untersuchungen an Aluminium, seinen Defekten und Aluminium-Legierungen*, PhD Thesis (2005), p.75

[Sc01] Schneider M.: *Studies for neutron tomography at the Institut Laue-Langevin*, diploma thesis, Heidelberg University (2001)

[Sc06] Schillinger B., Brunner J. et al.: *A study of oil lubrication in a rotating engine using stroboscopic neutron imaging*, Physica B 385-386 (2006) 921-923

[Si06] Sinha P.K., Halleck P., *Quantification of Liquid Water Saturation in a PEM Fuel Cell Diffusion Medium Using X-ray Microtomography*, Electrochemical and Solid-State Letters, 9 (2006) A344

[SN05] Swiss Neutron News, Swiss Neutron Scattering Society, Vol. 28 (2005), p. 25f

[Ta02] Tanaka E., Hatakeyama K. et al.: *Critical Supersaturation of Superfluid 3He-4He-Mixtures*, J. Low Temp. Phys. 127 (2002) 81

[Tr07] Trapp M., *Radiographische und tomographische Materialuntersuchungen bei hohen Neutronenflü ssen*, diploma thesis, Heidelberg University (2007)

[Vo06] Van Overberghe A. *High Flux Neutron Imaging for highly dynamic and time resolved non-destructive testing*, PhD thesis, Heidelberg University (2006)

[Vo07] Van Overberghe A.: *Simulation of the beam properties transmitted through the soller collimator and comparison of the beam with and without the collimator*, internal communications (2007)

[Wi67] Wilks J., *The properties of liquid and solid Helium*, Clarendon Press, Oxford (1967)

[Zi63] Zinov'eva K.N.: *Diagram of state for 3He-4He-solutions: phase stratification and solidification curves*, Sov. Phys. JETP 17 (1963) 1235

Appendix

A Table values for dilute 3He-4He-mixtures

	Heating power [mW]										
Temp [K]	0.005	0.01	0.02	0.04	0.08	0.16	0.32	0.64	1.28	2.56	5.12
0.40	2.0E-02	3.9E-02	7.9E-02	1.6E-01	3.2E-01	6.3E-01	1.3E+00	2.5E+00	5.0E+00	1.0E+01	2.0E+01
0.45	1.2E-02	2.5E-02	5.0E-02	9.9E-02	2.0E-01	4.0E-01	7.9E-01	1.6E+00	3.2E+00	6.4E+00	1.3E+01
0.50	8.2E-03	1.6E-02	3.3E-02	6.6E-02	1.3E-01	2.6E-01	5.3E-01	1.1E+00	2.1E+00	4.2E+00	8.4E+00
0.55	5.6E-03	1.1E-02	2.2E-02	4.5E-02	9.0E-02	1.8E-01	3.6E-01	7.2E-01	1.4E+00	2.9E+00	5.8E+00
0.60	5.2E-03	1.0E-02	2.1E-02	4.2E-02	8.4E-02	1.7E-01	3.4E-01	6.7E-01	1.3E+00	2.7E+00	5.4E+00
0.65	2.8E-03	5.6E-03	1.1E-02	2.2E-02	4.5E-02	8.9E-02	1.8E-01	3.6E-01	7.2E-01	1.4E+00	2.9E+00
0.70	2.0E-03	4.0E-03	7.9E-03	1.6E-02	3.2E-02	6.3E-02	1.3E-01	2.5E-01	5.1E-01	1.0E+00	2.0E+00
0.75	1.4E-03	2.8E-03	5.6E-03	1.1E-02	2.2E-02	4.5E-02	8.9E-02	1.8E-01	3.6E-01	7.1E-01	1.4E+00
0.80	9.7E-04	1.9E-03	3.9E-03	7.7E-03	1.5E-02	3.1E-02	6.2E-02	1.2E-01	2.5E-01	5.0E-01	9.9E-01
0.85	6.7E-04	1.3E-03	2.7E-03	5.3E-03	1.1E-02	2.1E-02	4.3E-02	8.5E-02	1.7E-01	3.4E-01	6.8E-01
0.90	4.6E-04	9.2E-04	1.8E-03	3.7E-03	7.3E-03	1.5E-02	2.9E-02	5.9E-02	1.2E-01	2.3E-01	4.7E-01
0.95	3.1E-04	6.2E-04	1.2E-03	2.5E-03	5.0E-03	9.9E-03	2.0E-02	4.0E-02	7.9E-02	1.6E-01	3.2E-01
1.00	2.1E-04	4.3E-04	8.5E-04	1.7E-03	3.4E-03	6.8E-03	1.4E-02	2.7E-02	5.4E-02	1.1E-01	2.2E-01
1.05	1.5E-04	2.9E-04	5.9E-04	1.2E-03	2.4E-03	4.7E-03	9.4E-03	1.9E-02	3.8E-02	7.5E-02	1.5E-01
1.10	1.0E-04	2.1E-04	4.1E-04	8.2E-04	1.6E-03	3.3E-03	6.6E-03	1.3E-02	2.6E-02	5.3E-02	1.1E-01
1.15	7.3E-05	1.5E-04	2.9E-04	5.9E-04	1.2E-03	2.3E-03	4.7E-03	9.4E-03	1.9E-02	3.8E-02	7.5E-02
1.20	5.3E-05	1.1E-04	2.1E-04	4.3E-04	8.5E-04	1.7E-03	3.4E-03	6.8E-03	1.4E-02	2.7E-02	5.5E-02
1.25	4.0E-05	7.9E-05	1.6E-04	3.2E-04	6.3E-04	1.3E-03	2.5E-03	5.1E-03	1.0E-02	2.0E-02	4.1E-02
1.30	3.0E-05	6.0E-05	1.2E-04	2.4E-04	4.8E-04	9.6E-04	1.9E-03	3.8E-03	7.6E-03	1.5E-02	3.1E-02
1.35	2.3E-05	4.6E-05	9.2E-05	1.8E-04	3.7E-04	7.4E-04	1.5E-03	2.9E-03	5.9E-03	1.2E-02	2.4E-02
1.40	1.8E-05	3.6E-05	7.1E-05	1.4E-04	2.8E-04	5.7E-04	1.1E-03	2.3E-03	4.6E-03	9.1E-03	1.8E-02
1.45	1.4E-05	2.8E-05	5.5E-05	1.1E-04	2.2E-04	4.4E-04	8.9E-04	1.8E-03	3.5E-03	7.1E-03	1.4E-02
1.50	1.1E-05	2.2E-05	4.4E-05	8.8E-05	1.8E-04	3.5E-04	7.0E-04	1.4E-03	2.8E-03	5.6E-03	1.1E-02

Table A.1: Velocities of the normalfluid component for different temperatures and heating power for the cylindrical experimental volume.

	Heating power [mW]										
Temp [K]	0.005	0.01	0.02	0.04	0.08	0.16	0.32	0.64	1.28	2.56	5.12
0.40	9.0E-04	9.0E-04	9.0E-04	9.0E-04	9.0E-04	9.0E-04	9.0E-04	9.1E-04	9.2E-04	9.3E-04	9.7E-04
0.45	9.0E-04	9.0E-04	9.0E-04	9.0E-04	9.0E-04	9.0E-04	9.1E-04	9.1E-04	9.3E-04	9.5E-04	1.0E-03
0.50	9.0E-04	9.0E-04	9.0E-04	9.0E-04	9.0E-04	9.0E-04	9.1E-04	9.1E-04	9.3E-04	9.6E-04	1.0E-03
0.55	9.0E-04	9.0E-04	9.0E-04	9.0E-04	9.0E-04	9.0E-04	9.1E-04	9.2E-04	9.3E-04	9.6E-04	1.0E-03
0.60	9.0E-04	9.0E-04	9.0E-04	9.0E-04	9.0E-04	9.1E-04	9.1E-04	9.3E-04	9.5E-04	1.0E-03	1.1E-03
0.65	9.0E-04	9.0E-04	9.0E-04	9.0E-04	9.0E-04	9.1E-04	9.1E-04	9.3E-04	9.6E-04	1.0E-03	1.1E-03
0.70	9.0E-04	9.0E-04	9.0E-04	9.0E-04	9.1E-04	9.1E-04	9.2E-04	9.4E-04	9.9E-04	1.1E-03	1.3E-03
0.75	9.0E-04	9.0E-04	9.0E-04	9.0E-04	9.1E-04	9.2E-04	9.3E-04	9.7E-04	1.0E-03	1.2E-03	1.5E-03
0.80	9.0E-04	9.0E-04	9.0E-04	9.1E-04	9.1E-04	9.2E-04	9.5E-04	1.0E-03	1.1E-03	1.3E-03	1.9E-03
0.85	9.0E-04	9.0E-04	9.0E-04	9.1E-04	9.2E-04	9.4E-04	9.7E-04	1.1E-03	1.2E-03	1.6E-03	2.5E-03
0.90	9.0E-04	9.0E-04	9.1E-04	9.1E-04	9.3E-04	9.5E-04	1.0E-03	1.1E-03	1.4E-03	2.0E-03	3.4E-03
0.95	9.0E-04	9.0E-04	9.1E-04	9.2E-04	9.4E-04	9.7E-04	1.0E-03	1.2E-03	1.6E-03	2.4E-03	4.5E-03
1.00	9.0E-04	9.1E-04	9.1E-04	9.2E-04	9.5E-04	9.9E-04	1.1E-03	1.3E-03	1.8E-03	3.0E-03	5.7E-03
1.05	9.0E-04	9.1E-04	9.2E-04	9.3E-04	9.7E-04	1.0E-03	1.2E-03	1.5E-03	2.3E-03	4.2E-03	8.2E-03
1.10	9.1E-04	9.1E-04	9.2E-04	9.5E-04	9.9E-04	1.1E-03	1.3E-03	1.8E-03	3.0E-03	5.7E-03	1.1E-02
1.15	9.1E-04	9.2E-04	9.3E-04	9.6E-04	1.0E-03	1.2E-03	1.5E-03	2.2E-03	3.9E-03	7.7E-03	1.5E-02
1.20	9.1E-04	9.2E-04	9.4E-04	9.9E-04	1.1E-03	1.3E-03	1.8E-03	2.9E-03	5.5E-03	1.1E-02	2.2E-02
1.25	9.2E-04	9.3E-04	9.6E-04	1.0E-03	1.2E-03	1.5E-03	2.2E-03	4.0E-03	7.8E-03	1.6E-02	3.1E-02
1.30	9.2E-04	9.4E-04	9.9E-04	1.1E-03	1.3E-03	1.7E-03	2.8E-03	5.4E-03	1.1E-02	2.1E-02	4.3E-02
1.35	9.3E-04	9.5E-04	1.0E-03	1.1E-03	1.4E-03	2.0E-03	3.5E-03	6.9E-03	1.4E-02	2.7E-02	5.5E-02
1.40	9.3E-04	9.6E-04	1.0E-03	1.2E-03	1.5E-03	2.2E-03	4.0E-03	8.0E-03	1.6E-02	3.2E-02	6.4E-02
1.45	9.3E-04	9.7E-04	1.0E-03	1.2E-03	1.5E-03	2.3E-03	4.3E-03	8.4E-03	1.7E-02	3.4E-02	6.8E-02
1.50	9.3E-04	9.7E-04	1.0E-03	1.2E-03	1.5E-03	2.3E-03	4.1E-03	8.2E-03	1.6E-02	3.3E-02	6.5E-02

Table A.2: Maximal concentration of 3He inside the cylindrical experimental volume as function of heating power and temperature. At ANTARES, the concentration should not exceed 3000ppm for sufficient neutron statistics

Temp [K]	Heating power [mW]										
	0.005	0.01	0.02	0.04	0.08	0.16	0.32	0.64	1.28	2.56	5.12
0.40	1.4E-04	2.8E-04	5.5E-04	1.1E-03	2.2E-03	4.4E-03	8.9E-03	1.8E-02	3.6E-02	7.3E-02	1.5E-01
0.45	2.2E-04	4.4E-04	8.8E-04	1.8E-03	3.5E-03	7.0E-03	1.4E-02	2.8E-02	5.8E-02	1.2E-01	2.5E-01
0.50	2.5E-04	5.0E-04	9.9E-04	2.0E-03	4.0E-03	8.0E-03	1.6E-02	3.2E-02	6.6E-02	1.4E-01	2.9E-01
0.55	2.7E-04	5.4E-04	1.1E-03	2.2E-03	4.4E-03	8.7E-03	1.8E-02	3.5E-02	7.2E-02	1.5E-01	3.2E-01
0.60	4.5E-04	9.0E-04	1.8E-03	3.6E-03	7.2E-03	1.4E-02	2.9E-02	5.9E-02	1.2E-01	2.6E-01	5.8E-01
0.65	4.8E-04	9.6E-04	1.9E-03	3.8E-03	7.7E-03	1.5E-02	3.1E-02	6.3E-02	1.3E-01	2.8E-01	6.3E-01
0.70	7.4E-04	1.5E-03	3.0E-03	5.9E-03	1.2E-02	2.4E-02	4.8E-02	9.9E-02	2.1E-01	4.6E-01	1.1E+00
0.75	1.2E-03	2.3E-03	4.7E-03	9.4E-03	1.9E-02	3.8E-02	7.8E-02	1.6E-01	3.5E-01	8.2E-01	2.3E+00
0.80	1.7E-03	3.4E-03	6.8E-03	1.4E-02	2.8E-02	5.6E-02	1.1E-01	2.4E-01	5.4E-01	1.4E+00	4.7E+00
0.85	2.5E-03	5.0E-03	1.0E-02	2.0E-02	4.1E-02	8.4E-02	1.7E-01	3.8E-01	9.0E-01	2.6E+00	1.2E+01
0.90	3.6E-03	7.2E-03	1.4E-02	2.9E-02	5.9E-02	1.2E-01	2.6E-01	5.8E-01	1.5E+00	5.3E+00	3.8E+01
0.95	4.9E-03	9.8E-03	2.0E-02	4.0E-02	8.1E-02	1.7E-01	3.7E-01	8.6E-01	2.5E+00	1.1E+01	1.4E+02
1.00	6.2E-03	1.3E-02	2.5E-02	5.1E-02	1.0E-01	2.2E-01	4.9E-01	1.2E+00	3.9E+00	2.3E+01	5.8E+02
1.05	9.0E-03	1.8E-02	3.6E-02	7.4E-02	1.5E-01	3.3E-01	7.7E-01	2.1E+00	8.9E+00	9.6E+01	9.5E+03
1.10	1.3E-02	2.5E-02	5.1E-02	1.0E-01	2.2E-01	4.9E-01	1.2E+00	3.9E+00	2.3E+01	5.8E+02	3.4E+05
1.15	1.7E-02	3.4E-02	6.9E-02	1.4E-01	3.0E-01	7.0E-01	1.9E+00	7.4E+00	7.0E+01	5.0E+03	2.5E+07
1.20	2.4E-02	4.9E-02	1.0E-01	2.1E-01	4.7E-01	1.1E+00	3.6E+00	2.0E+01	4.5E+02	2.1E+05	4.3E+10
1.25	3.5E-02	7.0E-02	1.5E-01	3.1E-01	7.2E-01	2.0E+00	7.8E+00	7.6E+01	6.0E+03	3.6E+07	1.3E+15
1.30	4.8E-02	9.7E-02	2.0E-01	4.5E-01	1.1E+00	3.4E+00	1.9E+01	3.8E+02	1.4E+05	2.1E+10	4.4E+20
1.35	6.1E-02	1.3E-01	2.7E-01	6.1E-01	1.6E+00	5.7E+00	4.4E+01	2.1E+03	4.2E+06	1.8E+13	3.2E+26
1.40	7.2E-02	1.5E-01	3.2E-01	7.4E-01	2.0E+00	8.2E+00	8.4E+01	7.2E+03	5.1E+07	2.6E+15	6.9E+30
1.45	7.6E-02	1.6E-01	3.4E-01	8.0E-01	2.2E+00	9.4E+00	1.1E+02	1.2E+04	1.4E+08	2.0E+16	3.8E+32
1.50	7.3E-02	1.5E-01	3.3E-01	7.6E-01	2.1E+00	8.7E+00	9.3E+01	8.8E+03	7.7E+07	5.9E+15	3.4E+31

Table A.3: Concentration difference between the bottom X(0) and the top X(h) of the experimental volume: The value (X(h)-X(0))/X(0), listed in the table, is independent from the concentration inside the cell.

Acknowledgements

I am very grateful to the people who supported me and my work on this thesis. In particular:

- My supervisor Prof. Dr. Hartmut Abele from the University of Heidelberg and Dr. Andreas Van Overberghe and Dr. Roland Gähler from ILL for their support and fruitful discussions
- Dr. Jürgen Peters and Heiner Kolb from the sample environment at FRM-II for their patience and their help to improve the helium experiments
- The ANTARES team, especially Dr. Burkhard Schillinger, Michael Schulz and Martin Mühlbauer
- Prof. Mike Hayden from the Simon Frazier University for interesting discussions about the experiment with dilute helium mixtures
- Axel Steuwer and Jens Altenkirch for their assistance during the experiment with aluminium alloys

And all other persons who supported me during my diploma thesis.

Declaration

I confirm that this work submitted for assessment is my own and expressed in my own words. Any use made within it of works of other authors in any form (e.g. ideas, figures, text, tables) are properly acknowledged at their point of use. A list of the references employed is included.

Signed

Date